

# Non-Hermitian skin effect enforced by nonsymmorphic symmetries

Yutaro Tanaka,<sup>1</sup> Ryo Takahashi,<sup>2</sup> and Ryo Okugawa<sup>3</sup>

<sup>1</sup>*Department of Physics, Tokyo Institute of Technology,  
2-12-1 Ookayama, Meguro-ku, Tokyo 152-8551, Japan*

<sup>2</sup>*Advanced Institute for Materials Research (WPI-AIMR), Tohoku University, Sendai 980-8577, Japan*

<sup>3</sup>*Department of Applied Physics, Tokyo University of Science, Tokyo 125-8585, Japan*

Crystal symmetries play an essential role in band structures of non-Hermitian Hamiltonian. In this letter, we propose a non-Hermitian skin effect (NHSE) enforced by nonsymmorphic symmetries. We show that the nonsymmorphic-symmetry-enforced NHSE inevitably occurs if a two-dimensional non-Hermitian system satisfies certain conditions characterized by nonsymmorphic symmetries. This NHSE can occur even in the presence of time-reversal symmetry. The nonsymmorphic-symmetry-enforced NHSE always occurs simultaneously with the closing of the point gap at zero energy. We also show that such a NHSE can occur in specific three-dimensional space groups with nonsymmorphic symmetries.

*Introduction.* Non-Hermiticity is universal in physics because open quantum and classical systems are effectively described as non-Hermitian matrices [1–12]. With recent experimental advances, non-Hermitian band structures have been intensively investigated. Intriguingly, non-Hermiticity allows unique non-Hermitian band topology without Hermitian counterparts [13, 14], *e.g.*, the non-Hermitian skin effect (NHSE) [15–43]. The NHSE is a drastic difference in energy spectrum between a periodic boundary condition (PBC) and an open boundary condition (OBC) [13, 14]. In particular, owing to the NHSEs, a systematic understanding of non-Hermitian band topology is still elusive in high-dimensional systems.

To understand the band structures, the concept of topological phases protected by crystal symmetries [44–64] has been applied to non-Hermitian systems. Previous works have revealed a relationship between non-Hermitian energy spectra and band topology through symmorphic symmetries, including inversion [65–70], mirror [69, 71], and rotation [69, 72–74]. In contrast, little has been done to examine the effects of nonsymmorphic symmetries (*e.g.* screw rotation and glide mirror) on non-Hermitian Hamiltonians although they add strong constraints to band structures in Hermitian systems, such as symmetry-enforced gaplessness [75–81].

In this letter, we propose a class of NHSEs enforced by nonsymmorphic symmetries. This NHSE necessarily occurs if a non-Hermitian Hamiltonian satisfies certain conditions of symmetry and matrix size. We also clarify how the conditions depend on the presence of time-reversal symmetry. We also show that when the nonsymmorphic-symmetry-enforced NHSE occurs, the point gap always closes at  $E = 0$  under the full PBC. The gap closing is a non-Hermitian counterpart of symmetry-enforced gaplessness in Hermitian systems. This NHSE can occur even in 2D systems with time-reversal symmetry defined with transposition although the time-reversal symmetry generally suppresses a 1D NHSE characterized by a winding number [19, 28, 82].

*Nonsymmorphic-symmetry-enforced NHSE with time-reversal symmetry.* To begin with, we explain the point-gap topology for NHSEs [15, 19, 21, 28]. A point gap at a wavevector  $\mathbf{k}$  is open at a reference energy  $E$  if the Hamiltonian  $H(\mathbf{k})$  satisfies  $\det[H(\mathbf{k}) - E] \neq 0$ . When the point gap is open at  $E$  on a line along the  $k_i$  ( $i = x, y, z$ ) direction, we can define a winding number along the  $k_i$  direction as

$$W_i(k_\perp) = \int_0^{2\pi} \frac{dk_i}{2\pi i} \frac{\partial}{\partial k_i} \log \det[H(\mathbf{k}) - E], \quad (1)$$

where  $k_\perp$  is the wave vector perpendicular to  $k_i$ . If  $W_i(k_\perp)$  is nonzero at a reference energy  $E$ , the NHSE occurs under the OBC in the  $i$  direction [15, 19, 28, 40]. Throughout this paper, we focus on the reference energy  $E = 0$ .

We consider a 2D non-Hermitian Hamiltonian in class AIII<sup>†</sup> with time-reversal symmetry  $\mathcal{T}H^T(\mathbf{k})\mathcal{T}^{-1} = H(-\mathbf{k})$ , where  $\mathcal{T}$  is a unitary matrix satisfying  $\mathcal{T}\mathcal{T}^* = -1$  [19]. We demonstrate the conditions under which a NHSE unavoidably occurs in the presence of the time-reversal symmetry. Initially, we assume that the matrix size of the Hamiltonian is  $N = 4M + 2$  with a nonnegative integer  $M$ . Additionally, we suppose that the Hamiltonian has the following generalized symmetry:

$$U_g^{\mathbf{k}} H(\mathbf{k}) = \left( U_g^{C_{2x}\mathbf{k}} H(C_{2x}\mathbf{k}) \right)^\dagger, \quad (2)$$

where  $C_{2x}$  represents the two-fold rotation around the  $x$  axis, *i.e.*  $C_{2x}\mathbf{k} = (k_x, -k_y)$ . Here  $U_g^{\mathbf{k}}$  is a unitary matrix defined as

$$U_g^{\mathbf{k}} := c_s e^{i\frac{k_x}{2}} A_g^{\mathbf{k}}, \quad (3)$$

where  $c_s = i(1)$  for  $C_{2x}^2 = -1(+1)$  in spinful (spinless) systems, and  $A_g^{\mathbf{k}}$  is an arbitrary  $(4M + 2) \times (4M + 2)$  unitary matrix that is periodic in the Brillouin zone. In addition, in the presence of time-reversal symmetry,  $U_g^{\mathbf{k}}$  needs to satisfy a relationship with  $\mathcal{T}$

$$\mathcal{T}(U_g^{\mathbf{k}})^* = -(U_g^{-C_{2x}\mathbf{k}})^\dagger \mathcal{T}. \quad (4)$$

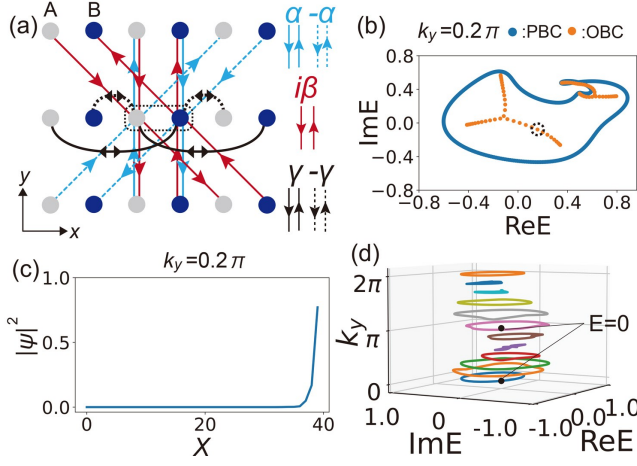


FIG. 1. Energy spectra of  $H_{2D}(\mathbf{k})$  with the parameters  $\alpha = \beta = 0.3$  and  $\gamma = 0.2$ . We take the PBC in the  $y$  direction for all the calculations. (a) Schematic diagram of our model in the real space. The dotted box indicates the unit cell. (b) The energy spectra on the  $k_y = 0.2\pi$  line under the PBC and the OBC in the  $x$  direction. (c) The spatial distributions of the skin mode in the dotted circle in (b). (d) The energy spectra in  $E$ - $k_y$  space under the full PBC.

As we discuss below, the generalized symmetry defined by Eq. (2) is associated with a screw rotation  $g = \{C_{2x}|\hat{x}/2\}$  symmetry, which is a twofold rotation  $C_{2x}$  followed by translation by a half of a lattice vector  $\hat{x}$ . Because the screw symmetry enforces NHSEs owing to the above condition, we refer to such NHSEs as nonsymmorphic-symmetry-enforced NHSEs. At the same time, the condition leads to the closing of the point gap on both  $k_y = 0$  and  $k_y = \pi$  lines under the full PBC.

For concreteness, we introduce a 2D two-band tight-binding model on a square lattice in class AIII $^\dagger$ :

$$H_{2D}(\mathbf{k}) = \begin{pmatrix} d(\mathbf{k}) & 2i\gamma \sin k_x \\ -2i\gamma \sin k_x & d(-\mathbf{k}) \end{pmatrix}, \quad (5)$$

where  $d(\mathbf{k}) = \alpha(1 - e^{-ik_x})e^{-ik_y} + i\beta(1 + e^{-ik_x})e^{ik_y}$ . The Hamiltonian in the real space is given in Sec. I of the Supplemental Material [83], and the model is time-reversal symmetric [82]:  $\sigma_y(H_{2D}(\mathbf{k}))^T(\mathbf{k})\sigma_y^{-1} = H_{2D}(-\mathbf{k})$ . The schematic diagram of this model in the real space is shown in Fig. 1(a). This model has two degrees of freedom  $A$  and  $B$  in the unit cells. The Hamiltonian  $H_{2D}(\mathbf{k})$  satisfies the condition in Eq. (2) with  $c_s = i$  and  $A_g^k = \text{diag}(1, -e^{-ik_x})$ . Figure 1(b) shows energy spectra of  $H_{2D}(\mathbf{k})$  on the  $k_y = 0.2\pi$  line both under the full PBC and under the OBC in the  $x$  direction. Figure 1(c) shows the eigenstate on the  $k_y = 0.2\pi$  line is localized at the right edge. These results indicate that a NHSE occurs in the model. Furthermore, the point gap closes at  $E = 0$  on the  $k_y = 0$  and  $k_y = \pi$  lines under the full PBC [Fig. 1(d)].

*Mechanism of nonsymmorphic-symmetry-enforced*

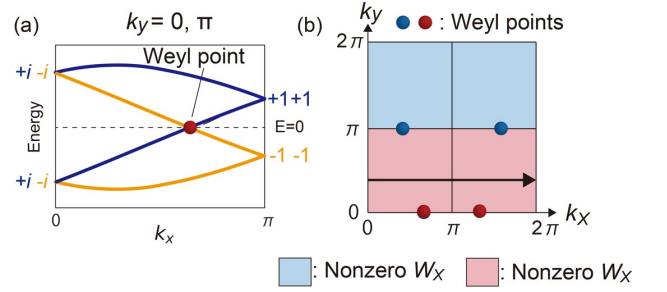


FIG. 2. (a) Schematic band structures of a doubled Hermitian Hamiltonian with  $\{C_{2x}|\hat{x}/2\}$  symmetry and time-reversal symmetry along the screw-invariant line. (b) Weyl points and regions with the nonzero winding number  $W_i(k_\perp)$  ( $i = x, y$ ). The colors of the nonzero  $W_x(k_y)$  regions indicate the opposite sign of the winding number:  $W_x(k_y) = -W_x(-k_y)$ . The arrow indicates the direction of the integration of  $W_i(k_\perp)$ . The red and blue points are Weyl points, and the color difference represents their opposite chirality.

*NHSE and gaplessness.* To understand why Eq. (2) leads to the NHSE, we introduce a doubled Hermitian Hamiltonian

$$\tilde{H}(\mathbf{k}) = \begin{pmatrix} 0 & H(\mathbf{k}) \\ H^\dagger(\mathbf{k}) & 0 \end{pmatrix}. \quad (6)$$

The point-gap topology of a non-Hermitian Hamiltonian  $H(\mathbf{k})$  corresponds to the band topology of the doubled Hermitian Hamiltonian  $\tilde{H}(\mathbf{k})$ , which has chiral symmetry [15, 19, 84, 85]. The chiral symmetry is described as  $\Gamma\tilde{H}(\mathbf{k})\Gamma^{-1} = -\tilde{H}(\mathbf{k})$  with  $\Gamma = \text{diag}(\mathbf{1}_N, -\mathbf{1}_N)$ , where  $\mathbf{1}_N$  is the  $N \times N$  identity matrix. In particular, we can diagnose whether the winding number  $W_i(k_\perp)$  is nonzero from information on the topology of the doubled Hermitian Hamiltonian (see Sec. II of the Supplemental Material [83] for details of the connection between the topology of  $\tilde{H}(\mathbf{k})$  and  $W_i(k_\perp)$ ).

As we show in Sec. III of the Supplemental Material [83], if  $H(\mathbf{k})$  satisfies the condition in Eq. (2),  $\tilde{H}(\mathbf{k})$  has the screw rotation symmetry  $g = \{C_{2x}|\hat{x}/2\}$ . Thus, eigenstates of  $\tilde{H}(\mathbf{k})$  have the screw rotation eigenvalues  $\pm c_s e^{-i\frac{k_x}{2}}$  on the screw-invariant lines ( $k_y = 0, \pi$ ). Here we consider a case with  $C_{2x}^2 = -1$  ( $c_s = i$ ). Also, when Eq. (4) holds, the doubled Hermitian Hamiltonian  $\tilde{H}(\mathbf{k})$  has time-reversal symmetry  $\tilde{T}\tilde{H}(\mathbf{k})\tilde{T}^{-1} = \tilde{H}(-\mathbf{k})$ , where  $\tilde{T}^2 = -1$  (for the details of the derivation of the relationship, see Sec. IV of the Supplemental Material [83]). Because of the time-reversal symmetry, while Kramers pairs at  $k_x = 0$  have opposite screw rotation eigenvalues  $\pm i$ , Kramers pairs at  $k_x = \pi$  have the same eigenvalues [Fig. 2(a)]. Since the symmetry eigenvalues must exchange on the line, the eigenstates enforce Weyl points on the screw-invariant line [75, 86]. Because the number of bands of  $\tilde{H}(\mathbf{k})$  is  $8M + 4$  by assumption, the chiral symmetry fixes the 2D Weyl points at zero energy. The emergent Weyl points give a path with a nonzero winding

Symmetry class	Matrix size of $H(\mathbf{k})$ and $A_g^{\mathbf{k}}$	Relation between $\mathcal{T}$ and $U_g^{\mathbf{k}}$
class A	$2M + 1$	–
class AII	$4M + 2$	$\mathcal{T}(U_g^{\mathbf{k}})^* = -U_g^{-\mathbf{k}}\mathcal{T}$
class AII <sup>†</sup>	$4M + 2$	$\mathcal{T}(U_g^{\mathbf{k}})^* = -(U_g^{-C_{2x}\mathbf{k}})^{\dagger}\mathcal{T}$

TABLE I. Conditions of the matrix size and the symmetries for nonsymmorphic-symmetry-enforced NHSEs. When a given non-Hermitian Hamiltonian satisfies the conditions of the symmetry and the matrix size, the system can realize symmetry-enforced NHSEs.

number in the Brillouin zone, depending on their chirality and positions [85, 87–90].

When the doubled Hermitian Hamiltonian  $\tilde{H}(\mathbf{k})$  has a nonzero winding number, the non-Hermitian Hamiltonian  $H(\mathbf{k})$  also has nonzero  $W_i(k_{\perp})$ , as discussed above. Thus, corresponding to the 2D Weyl points enforced by the screw symmetry, the non-Hermitian Hamiltonian  $H(\mathbf{k})$  has a nonzero winding number [Fig. 2(b)]. A time-reversal pair of the Weyl points on the screw-invariant line has the same chirality [Fig. 2(b)] (for the proof, see Sec. II of the Supplemental Material [83]). In addition, the winding number satisfies  $W_x(-k_y) = -W_x(k_y)$  because  $\mathcal{T}H^T(\mathbf{k})\mathcal{T}^{-1} = H(-\mathbf{k})$ . Thus, the winding number  $W_x(k_y)$  is nonzero at any  $k_y$  due to the positions and the chirality of the Weyl points [Fig. 2(b)].

Moreover, since the 2D Weyl points appear at zero energy, we obtain  $\det[H(\mathbf{k})]\det[H^{\dagger}(\mathbf{k})] = 0$  at some wavevector on the screw-invariant lines. Therefore, the point-gap closing of  $H(\mathbf{k})$  is found at  $E = 0$  under the full PBC. Thus, the nonsymmorphic-symmetry-enforced NHSE always occurs with the point-gap closing on the screw-invariant lines.

*Nonsymmorphic-symmetry-enforced NHSE in other symmetry classes.* Next, we discuss nonsymmorphic-symmetry-enforced NHSEs in symmetry class A and class AII. Non-Hermitian Hamiltonians in class A do not have any internal symmetries. Meanwhile, non-Hermitian Hamiltonians  $H(\mathbf{k})$  in symmetry class AII have time-reversal symmetry  $\mathcal{T}H^*(\mathbf{k})\mathcal{T}^{-1} = H(-\mathbf{k})$ , where  $\mathcal{T}$  is a unitary matrix satisfying  $\mathcal{T}\mathcal{T}^* = -1$  [19]. As discussed in Sec. IV of the Supplemental Material [83], Eq. (2) is also applied to class A and class AII. In the presence of time-reversal symmetry in class AII,  $U_g^{\mathbf{k}}$  needs to satisfy a relationship with  $\mathcal{T}$  in Table I. In contrast, NHSEs in 2D Hamiltonians in class AI and class AI<sup>†</sup> are not enforced. The derivation of the above results is given in Sec. IV of the Supplemental Material [83].

Furthermore, we discuss the matrix size of non-Hermitian Hamiltonians  $H(\mathbf{k})$  to realize symmetry-enforced NHSEs. To see the conditions of the matrix size we investigate Weyl points of the doubled Hermitian Hamiltonians  $\tilde{H}(\mathbf{k})$  with the screw symmetry and with/without time-reversal symmetry. The details of the

band topology are given in Secs. III and IV of the Supplemental Material [83]. When the matrix size of  $H(\mathbf{k})$  in class A is  $2M + 1$ ,  $H(\mathbf{k})$  has a 2D Weyl point on the screw invariant lines. On the other hand, when the matrix size of  $H(\mathbf{k})$  in class AII is  $4M + 2$ ,  $\tilde{H}(\mathbf{k})$  has a pair of 2D Weyl points on the screw invariant lines. These results are summarized in Table I.

*3D nonsymmorphic-symmetry-enforced NHSE.* While nonsymmorphic-symmetry-enforced NHSEs cannot be realized in 2D systems in class AI, they can occur in 3D systems in class AI. To show this, let us extend the above discussion for 2D systems to that for 3D systems. We introduce a 3D two-band non-Hermitian model on a primitive orthorhombic lattice. The model is given by

$$H_{3D}(\mathbf{k}) = v_0(\mathbf{k})\sigma_0 + \sum_{i=x,y} v_i(\mathbf{k})\sigma_i, \quad (7)$$

and the coefficient functions are given by

$$\begin{aligned} v_0(\mathbf{k}) &= t_0 f_1(\mathbf{k}_{\parallel}) - it_a \sin k_z f_1(\mathbf{k}_{\parallel}), \\ v_x(\mathbf{k}) &= -it_b \sin k_z f_1(\mathbf{k}_{\parallel}) - it_c \sin k_z f_2(\mathbf{k}_{\parallel}) \\ &\quad + t_d(1 - \cos k_z) f_2(\mathbf{k}_{\parallel}), \\ v_y(\mathbf{k}) &= -it_b(1 - \cos k_z) f_1(\mathbf{k}_{\parallel}) + it_c(1 + \cos k_z) f_2(\mathbf{k}_{\parallel}) \\ &\quad - t_d \sin k_z f_2(\mathbf{k}_{\parallel}), \end{aligned} \quad (8)$$

where  $\mathbf{k}_{\parallel} = (k_x, k_y)$  is the  $x$ - $y$  plane momentum,  $f_1(\mathbf{k}_{\parallel}) = (1 + e^{-ik_x})(1 + e^{-ik_y})$ , and  $f_2(\mathbf{k}_{\parallel}) = (e^{ik_x} - e^{-2ik_x})(1 - e^{-ik_y}) - (e^{ik_y} - e^{-2ik_y})(1 - e^{-ik_x})$ . This model has time-reversal symmetry:  $H_{3D}^*(\mathbf{k}) = H_{3D}(-\mathbf{k})$ , and therefore it belongs to class AI. We calculate energy spectra of  $H_{3D}(\mathbf{k})$  under the PBC in both the  $x$  and the  $y$  directions. Figure 3(a) shows that the NHSE occurs under the OBC in the  $z$  direction. Then Fig. 3(b) shows that the eigenstates are localized at the surface normal to the  $z$  direction.

To understand the origin of the NHSE, we discuss band structures of the doubled Hermitian Hamiltonian  $\tilde{H}_{3D}(\mathbf{k})$  obtained from  $H_{3D}(\mathbf{k})$ . The doubled Hermitian Hamiltonian  $\tilde{H}_{3D}(\mathbf{k})$  belongs to  $P4/ncc$  (No. 130) space group with nonsymmorphic symmetries (for the details of relationships between the symmetries and band structures of  $\tilde{H}_{3D}(\mathbf{k})$ , see Sec. V of the Supplemental Material [83]). If the matrix size of  $H_{3D}(\mathbf{k})$  is  $4M + 2$ , the crystal symmetries enforce the emergence of nodal lines on the  $k_z = \pi$  plane in the presence of time-reversal symmetry [81]. Importantly, nodal lines generally lead to a path with a non-trivial winding number in the 3D Brillouin zone [91–95]. In this case, a winding number calculated along the  $k_z$  direction changes its value on the nodal line. Thus, the corresponding non-Hermitian Hamiltonian  $H_{3D}(\mathbf{k})$  has a nonzero winding number  $W_z(\mathbf{k}_{\parallel})$ , as shown in Fig. 3(c). As a result, we see that a symmetry-enforced NHSE happens in 3D non-Hermitian lattices.

Also, we find that the point gap closes at  $E = 0$  on specific lines along the  $k_z$  direction under the full PBC

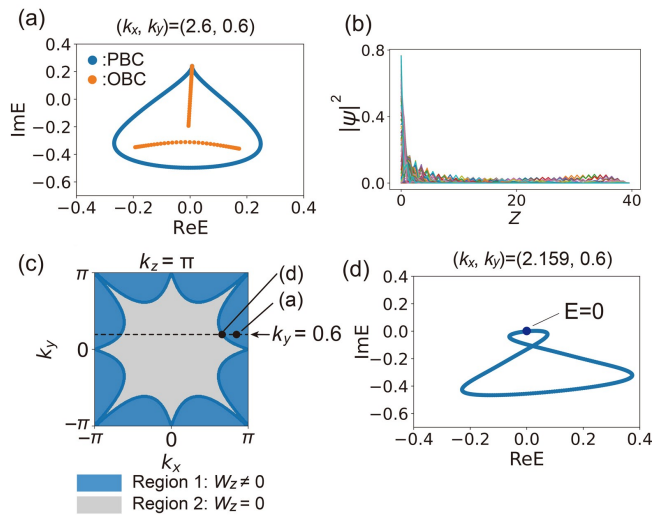


FIG. 3. Nonsymmorphic-symmetry-enforced NHSEs in the 3D system. We choose the parameters  $t_0 = 0.125$ ,  $t_a = 0.1$ ,  $t_b = t_d = 0.05$ , and  $t_c = 0.025$ . (a) The energy spectra of  $H_{3D}(\mathbf{k})$  with  $(k_x, k_y) = (2.6, 0.6)$  under the PBC in the  $z$  direction and the OBC in the  $z$  direction. (b) The spatial distributions for all the right eigenstates at  $(k_x, k_y) = (2.6, 0.6)$ . The system size in the  $z$  direction is 40. (c) Top view of the winding number  $W_z(\mathbf{k}_{\parallel})$  on the  $k_x$ - $k_y$  space. The winding number varies on the nodal line on the  $k_z = \pi$  plane. (d) The energy spectra with  $(k_x, k_y) = (2.159, 0.6)$  calculated along the  $k_z$  direction under the full PBC.

[Fig. 3(d)]. We can also grasp the point-gap closing at  $E = 0$  from the symmetry-enforced nodal line. Because of chiral symmetry,  $\tilde{H}_{3D}(\mathbf{k})$  hosts the nodal line at zero energy. Hence, similar to the 2D cases with symmetry-enforced Weyl points,  $H_{3D}(\mathbf{k})$  shows the point-gap closing at  $E = 0$  on the wave vector where the nodal line appears.

*Conclusions.* In summary, we study NHSEs enforced by nonsymmorphic symmetry in 2D and 3D non-Hermitian systems, which we call nonsymmorphic-symmetry-enforced NHSEs. We have clarified the conditions of symmetry and matrix size of non-Hermitian Hamiltonians for the NHSEs. If the conditions are satisfied, these NHSEs inevitably happen. We have also unveiled that the point gap at  $E = 0$  closes under the full PBC when the NHSEs occur. These NHSEs can occur in 2D systems not only without time-reversal symmetry but also with time-reversal symmetry. We especially show that the NHSEs occur even in symmetry class AII<sup>†</sup>.

NHSEs have been experimentally observed in artificially designed systems [82, 96–103]. We believe that our theory can be readily confirmed in artificial two-dimensional systems, such as active matter [102] and electric circuits [82, 103]. In addition, these artificial platforms are easier to design symmetries of the systems than electronic systems. Our theory guides to design non-Hermitian band structures in terms of spatial sym-

metries.

*Acknowledgments.*— This work was supported by Japan Society for the Promotion of Science (JSPS) KAKENHI Grant No. JP20H01845, No. JP21J22264, and No. JP23K13033.

- [1] G. Gamow, Zur Quantentheorie des Atomkernes, *Z. für Phys.* **51**, 204 (1928).
- [2] A. J. F. Siegert, On the Derivation of the Dispersion Formula for Nuclear Reactions, *Phys. Rev.* **56**, 750 (1939).
- [3] H. Feshbach, Unified theory of nuclear reactions, *Annals of Physics* **5**, 357 (1958).
- [4] H. Feshbach, A unified theory of nuclear reactions. II, *Annals of Physics* **19**, 287 (1962).
- [5] C. L. Kane and T. C. Lubensky, Topological boundary modes in isostatic lattices, *Nat. Phys.* **10**, 39 (2014).
- [6] S. D. Huber, Topological mechanics, *Nat. Phys.* **12**, 621 (2016).
- [7] V. V. Konotop, J. Yang, and D. A. Zezyulin, Nonlinear waves in  $\mathcal{PT}$ -symmetric systems, *Rev. Mod. Phys.* **88**, 035002 (2016).
- [8] L. Feng, R. El-Ganainy, and L. Ge, Non-Hermitian photonics based on parity–time symmetry, *Nat. Photon.* **11**, 752 (2017).
- [9] R. El-Ganainy, K. G. Makris, M. Khajavikhan, Z. H. Musslimani, S. Rotter, and D. N. Christodoulides, Non-Hermitian physics and PT symmetry, *Nat. Phys.* **14**, 11 (2018).
- [10] V. Kozii and L. Fu, Non-Hermitian topological theory of finite-lifetime quasiparticles: prediction of bulk Fermi arc due to exceptional point, arXiv:1708.05841 (2017).
- [11] H. Shen and L. Fu, Quantum Oscillation from In-Gap States and a Non-Hermitian Landau Level Problem, *Phys. Rev. Lett.* **121**, 026403 (2018).
- [12] M. Papaj, H. Isobe, and L. Fu, Nodal arc of disordered Dirac fermions and non-Hermitian band theory, *Phys. Rev. B* **99**, 201107(R) (2019).
- [13] Y. Ashida, Z. Gong, and M. Ueda, Non-Hermitian physics, *Advances in Physics* **69**, 249 (2020).
- [14] E. J. Bergholtz, J. C. Budich, and F. K. Kunst, Exceptional topology of non-Hermitian systems, *Rev. Mod. Phys.* **93**, 015005 (2021).
- [15] Z. Gong, Y. Ashida, K. Kawabata, K. Takasan, S. Higashikawa, and M. Ueda, Topological Phases of Non-Hermitian Systems, *Phys. Rev. X* **8**, 031079 (2018).
- [16] S. Yao and Z. Wang, Edge States and Topological Invariants of Non-Hermitian Systems, *Phys. Rev. Lett.* **121**, 086803 (2018).
- [17] S. Yao, F. Song, and Z. Wang, Non-Hermitian Chern Bands, *Phys. Rev. Lett.* **121**, 136802 (2018).
- [18] F. K. Kunst, E. Edvardsson, J. C. Budich, and E. J. Bergholtz, Biorthogonal Bulk-Boundary Correspondence in Non-Hermitian Systems, *Phys. Rev. Lett.* **121**, 026808 (2018).
- [19] K. Kawabata, K. Shiozaki, M. Ueda, and M. Sato, Symmetry and Topology in Non-Hermitian Physics, *Phys. Rev. X* **9**, 041015 (2019).
- [20] C. H. Lee and R. Thomale, Anatomy of skin modes and topology in non-Hermitian systems, *Phys. Rev. B* **99**,

- 201103(R) (2019).
- [21] H. Zhou and J. Y. Lee, Periodic table for topological bands with non-hermitian symmetries, *Phys. Rev. B* **99**, 235112 (2019).
- [22] C. H. Lee, L. Li, and J. Gong, Hybrid Higher-Order Skin-Topological Modes in Nonreciprocal Systems, *Phys. Rev. Lett.* **123**, 016805 (2019).
- [23] K. Yokomizo and S. Murakami, Non-Bloch Band Theory of Non-Hermitian Systems, *Phys. Rev. Lett.* **123**, 066404 (2019).
- [24] F. Song, S. Yao, and Z. Wang, Non-Hermitian Skin Effect and Chiral Damping in Open Quantum Systems, *Phys. Rev. Lett.* **123**, 170401 (2019).
- [25] F. Song, S. Yao, and Z. Wang, Non-Hermitian Topological Invariants in Real Space, *Phys. Rev. Lett.* **123**, 246801 (2019).
- [26] S. Longhi, Probing non-Hermitian skin effect and non-Bloch phase transitions, *Phys. Rev. Research* **1**, 023013 (2019).
- [27] D. S. Borgnia, A. J. Kruchkov, and R.-J. Slager, Non-Hermitian Boundary Modes and Topology, *Phys. Rev. Lett.* **124**, 056802 (2020).
- [28] N. Okuma, K. Kawabata, K. Shiozaki, and M. Sato, Topological origin of non-hermitian skin effects, *Phys. Rev. Lett.* **124**, 086801 (2020).
- [29] K. Kawabata, N. Okuma, and M. Sato, Non-Bloch band theory of non-Hermitian Hamiltonians in the symplectic class, *Phys. Rev. B* **101**, 195147 (2020).
- [30] K. Zhang, Z. Yang, and C. Fang, Correspondence between Winding Numbers and Skin Modes in Non-Hermitian Systems, *Phys. Rev. Lett.* **125**, 126402 (2020).
- [31] K. Yokomizo and S. Murakami, Non-bloch band theory in bosonic bogoliubov-de gennes systems, *Phys. Rev. B* **103**, 165123 (2021).
- [32] F. Schindler and A. Prem, Dislocation non-Hermitian skin effect, *Phys. Rev. B* **104**, L161106 (2021).
- [33] K. Yokomizo and S. Murakami, Scaling rule for the critical non-Hermitian skin effect, *Phys. Rev. B* **104**, 165117 (2021).
- [34] Y.-X. Xiao and C. T. Chan, Topology in non-hermitian chern insulators with skin effect, *Phys. Rev. B* **105**, 075128 (2022).
- [35] K. Yokomizo, T. Yoda, and S. Murakami, Non-Hermitian waves in a continuous periodic model and application to photonic crystals, *Phys. Rev. Research* **4**, 023089 (2022).
- [36] K. Deng and B. Flebus, Non-Hermitian skin effect in magnetic systems, *Phys. Rev. B* **105**, L180406 (2022).
- [37] S. Longhi, Non-Hermitian skin effect and self-acceleration, *Phys. Rev. B* **105**, 245143 (2022).
- [38] Q. Liang, D. Xie, Z. Dong, H. Li, H. Li, B. Gadway, W. Yi, and B. Yan, Dynamic Signatures of Non-Hermitian Skin Effect and Topology in Ultracold Atoms, *Phys. Rev. Lett.* **129**, 070401 (2022).
- [39] S. Franca, V. Könye, F. Hassler, J. van den Brink, and C. Fulga, Non-Hermitian Physics without Gain or Loss: The Skin Effect of Reflected Waves, *Phys. Rev. Lett.* **129**, 086601 (2022).
- [40] K. Zhang, Z. Yang, and C. Fang, Universal non-Hermitian skin effect in two and higher dimensions, *Nat. Commun.* **13**, 2496 (2022).
- [41] Y. Jin, W. Zhong, R. Cai, X. Zhuang, Y. Pennec, and B. Djafari-Rouhani, Non-Hermitian skin effect in a phononic beam based on piezoelectric feedback control, *Appl. Phys. Lett.* **121**, 022202 (2022).
- [42] F. Alsallom, L. Herviou, O. V. Yazyev, and M. Brzezińska, Fate of the non-Hermitian skin effect in many-body fermionic systems, *Phys. Rev. Research* **4**, 033122 (2022).
- [43] K. Kawabata, T. Numasawa, and S. Ryu, Entanglement Phase Transition Induced by the Non-Hermitian Skin Effect, *Phys. Rev. X* **13**, 021007 (2023).
- [44] L. Fu, Topological Crystalline Insulators, *Phys. Rev. Lett.* **106**, 106802 (2011).
- [45] C. Fang, M. J. Gilbert, X. Dai, and B. A. Bernevig, Multi-Weyl Topological Semimetals Stabilized by Point Group Symmetry, *Phys. Rev. Lett.* **108**, 266802 (2012).
- [46] T. H. Hsieh, H. Lin, J. Liu, W. Duan, A. Bansil, and L. Fu, Topological crystalline insulators in the SnTe material class, *Nat. Commun.* **3**, 982 (2012).
- [47] A. Alexandradinata, X. Dai, and B. A. Bernevig, Wilson-loop characterization of inversion-symmetric topological insulators, *Phys. Rev. B* **89**, 155114 (2014).
- [48] S. Murakami, M. Hirayama, R. Okugawa, and T. Miyake, Emergence of topological semimetals in gap closing in semiconductors without inversion symmetry, *Sci. Adv.* **3**, e1602680 (2017).
- [49] Z. Song, Z. Fang, and C. Fang,  $(d - 2)$ -Dimensional Edge States of Rotation Symmetry Protected Topological States, *Phys. Rev. Lett.* **119**, 246402 (2017).
- [50] F. Schindler, A. M. Cook, M. G. Vergniory, Z. Wang, S. S. Parkin, B. A. Bernevig, and T. Neupert, Higher-order topological insulators, *Sci. Adv.* **4**, eaat0346 (2018).
- [51] E. Khalaf, Higher-order topological insulators and superconductors protected by inversion symmetry, *Phys. Rev. B* **97**, 205136 (2018).
- [52] E. Khalaf, H. C. Po, A. Vishwanath, and H. Watanabe, Symmetry Indicators and Anomalous Surface States of Topological Crystalline Insulators, *Phys. Rev. X* **8**, 031070 (2018).
- [53] C. Fang and L. Fu, New classes of topological crystalline insulators having surface rotation anomaly, *Sci. Adv.* **5**, eaat2374 (2019).
- [54] Y. Tanaka, R. Takahashi, and S. Murakami, Appearance of hinge states in second-order topological insulators via the cutting procedure, *Phys. Rev. B* **101**, 115120 (2020).
- [55] R. Takahashi, Y. Tanaka, and S. Murakami, Bulk-edge and bulk-hinge correspondence in inversion-symmetric insulators, *Phys. Rev. Research* **2**, 013300 (2020).
- [56] L. He, Z. Addison, E. J. Mele, and B. Zhen, Quadrupole topological photonic crystals, *Nat. Commun.* **11**, 1 (2020).
- [57] Y. Tanaka, R. Takahashi, T. Zhang, and S. Murakami, Theory of inversion- $\mathbb{Z}_4$  protected topological chiral hinge states and its applications to layered antiferromagnets, *Phys. Rev. Research* **2**, 043274 (2020).
- [58] H. Kim, H. Cheng, L. Lu, and S. Murakami, Theoretical analysis of glide- $\mathbb{Z}_2$  magnetic topological photonic crystals, *Opt. Express* **29**, 31164 (2021).
- [59] Y. Quan, V. Taufour, and W. E. Pickett, Nonsymmetric band sticking in a topological superconductor, *Phys. Rev. B* **105**, 064517 (2022).
- [60] Y. Tanaka, R. Takahashi, R. Okugawa, and S. Murakami, Rotoinversion-symmetric bulk-hinge correspondence and its applications to higher-order weyl semimetals, *Phys. Rev. B* **105**, 115119 (2022).

- [61] H. Xue, Z. Wang, Y.-X. Huang, Z. Cheng, L. Yu, Y. X. Foo, Y. X. Zhao, S. A. Yang, and B. Zhang, Projectively Enriched Symmetry and Topology in Acoustic Crystals, *Phys. Rev. Lett.* **128**, 116802 (2022).
- [62] Y. Tanaka, T. Zhang, M. Uwaha, and S. Murakami, Anomalous Crystal Shapes of Topological Crystalline Insulators, *Phys. Rev. Lett.* **129**, 046802 (2022).
- [63] C. Wang, F. Liu, and H. Huang, Effective Model for Fractional Topological Corner Modes in Quasicrystals, *Phys. Rev. Lett.* **129**, 056403 (2022).
- [64] Y. Tanaka and S. Murakami, Effects of first- and second-order topological phases on the equilibrium crystal shapes, arXiv:2304.08150 (2023).
- [65] R. Okugawa and T. Yokoyama, Topological exceptional surfaces in non-Hermitian systems with parity-time and parity-particle-hole symmetries, *Phys. Rev. B* **99**, 041202(R) (2019).
- [66] R. Okugawa, R. Takahashi, and K. Yokomizo, Second-order topological non-Hermitian skin effects, *Phys. Rev. B* **102**, 241202(R) (2020).
- [67] R. Okugawa, R. Takahashi, and K. Yokomizo, Non-Hermitian band topology with generalized inversion symmetry, *Phys. Rev. B* **103**, 205205 (2021).
- [68] P. M. Vecsei, M. M. Denner, T. Neupert, and F. Schindler, Symmetry indicators for inversion-symmetric non-Hermitian topological band structures, *Phys. Rev. B* **103**, L201114 (2021).
- [69] K. Shiozaki and S. Ono, Symmetry indicator in non-Hermitian systems, *Phys. Rev. B* **104**, 035424 (2021).
- [70] T. Yoshida, R. Okugawa, and Y. Hatsugai, Discriminant indicators with generalized inversion symmetry, *Phys. Rev. B* **105**, 085109 (2022).
- [71] T. Yoshida, T. Mizoguchi, and Y. Hatsugai, Mirror skin effect and its electric circuit simulation, *Phys. Rev. Research* **2**, 022062(R) (2020).
- [72] K. Kawabata, M. Sato, and K. Shiozaki, Higher-order non-Hermitian skin effect, *Phys. Rev. B* **102**, 205118 (2020).
- [73] W. B. Rui, Z. Zheng, C. Wang, and Z. D. Wang, Non-Hermitian Spatial Symmetries and Their Stabilized Normal and Exceptional Topological Semimetals, *Phys. Rev. Lett.* **128**, 226401 (2022).
- [74] H. Wakao, T. Yoshida, and Y. Hatsugai, Discriminant indicator with generalized rotational symmetry, *Phys. Rev. B* **105**, 214103 (2022).
- [75] S. M. Young and C. L. Kane, Dirac Semimetals in Two Dimensions, *Phys. Rev. Lett.* **115**, 126803 (2015).
- [76] B. J. Wieder and C. L. Kane, Spin-orbit semimetals in the layer groups, *Phys. Rev. B* **94**, 155108 (2016).
- [77] T. Bzdušek, Q. Wu, A. Rüegg, M. Sigrist, and A. A. Soluyanov, Nodal-chain metals, *Nature* **538**, 75 (2016).
- [78] Y. Chen, H.-S. Kim, and H.-Y. Kee, Topological crystalline semimetals in nonsymmorphic lattices, *Phys. Rev. B* **93**, 155140 (2016).
- [79] R. Chen, H. C. Po, J. B. Neaton, and A. Vishwanath, Topological materials discovery using electron filling constraints, *Nat. Phys.* **14**, 55 (2018).
- [80] H. Watanabe, H. C. Po, M. P. Zaletel, and A. Vishwanath, Filling-Enforced Gaplessness in Band Structures of the 230 Space Groups, *Phys. Rev. Lett.* **117**, 096404 (2016).
- [81] R. Takahashi, M. Hirayama, and S. Murakami, Spinless hourglass nodal-line semimetals, *Phys. Rev. B* **96**, 155206 (2017).
- [82] T. Hofmann, T. Helbig, F. Schindler, N. Salgo, M. Brzezińska, M. Greiter, T. Kiessling, D. Wolf, A. Vollhardt, A. Kabaš, C. H. Lee, A. Bilušić, R. Thomale, and T. Neupert, Reciprocal skin effect and its realization in a topoelectrical circuit, *Phys. Rev. Research* **2**, 023265 (2020).
- [83] See the Supplemental Material at URL for further details on our tight-binding model, the connection between the topology of the doubled Hermitian Hamiltonian and the winding number, the proof that Eq. (2) leads to the screw rotation symmetry of the doubled Hermitian Hamiltonian, the conditions to enforce NHSEs in class A and class AII, and the band structures and the symmetries of the doubled Hermitian Hamiltonian  $\tilde{H}_{3D}(\mathbf{k})$ , which includes Ref. [104].
- [84] A. P. Schnyder, S. Ryu, A. Furusaki, and A. W. W. Ludwig, Classification of topological insulators and superconductors in three spatial dimensions, *Phys. Rev. B* **78**, 195125 (2008).
- [85] C.-K. Chiu, J. C. Y. Teo, A. P. Schnyder, and S. Ryu, Classification of topological quantum matter with symmetries, *Rev. Mod. Phys.* **88**, 035005 (2016).
- [86] L. Michel and J. Zak, Connectivity of energy bands in crystals, *Phys. Rev. B* **59**, 5998 (1999).
- [87] S. Matsuura, P.-Y. Chang, A. P. Schnyder, and S. Ryu, Protected boundary states in gapless topological phases, *New J. of Phys.* **15**, 065001 (2013).
- [88] J. Ahn and B.-J. Yang, Unconventional Topological Phase Transition in Two-Dimensional Systems with Space-Time Inversion Symmetry, *Phys. Rev. Lett.* **118**, 156401 (2017).
- [89] W.-W. Yu, Y. Liu, W. Meng, H. Liu, J. Gao, X. Zhang, and G. Liu, Phononic higher-order nodal point in two dimensions, *Phys. Rev. B* **105**, 035429 (2022).
- [90] C. Le, Z. Yang, F. Cui, A. P. Schnyder, and C.-K. Chiu, Generalized fermion doubling theorems: Classification of two-dimensional nodal systems in terms of wallpaper groups, *Phys. Rev. B* **106**, 045126 (2022).
- [91] A. A. Burkov, M. D. Hook, and L. Balents, Topological nodal semimetals, *Phys. Rev. B* **84**, 235126 (2011).
- [92] M. Phillips and V. Aji, Tunable line node semimetals, *Phys. Rev. B* **90**, 115111 (2014).
- [93] C. Fang, Y. Chen, H.-Y. Kee, and L. Fu, Topological nodal line semimetals with and without spin-orbital coupling, *Phys. Rev. B* **92**, 081201(R) (2015).
- [94] L. S. Xie, L. M. Schoop, E. M. Seibel, Q. D. Gibson, W. Xie, and R. J. Cava, A new form of Ca<sub>3</sub>P<sub>2</sub> with a ring of Dirac nodes, *APL Mater.* **3**, 083602 (2015).
- [95] Y. Kim, B. J. Wieder, C. L. Kane, and A. M. Rappe, Dirac Line Nodes in Inversion-Symmetric Crystals, *Phys. Rev. Lett.* **115**, 036806 (2015).
- [96] L. Xiao, T. Deng, K. Wang, G. Zhu, Z. Wang, W. Yi, and P. Xue, Non-Hermitian bulk–boundary correspondence in quantum dynamics, *Nat. Phys.* **16**, 761 (2020).
- [97] S. Weidemann, M. Kremer, T. Helbig, T. Hofmann, A. Stegmaier, M. Greiter, R. Thomale, and A. Szameit, Topological funneling of light, *Science* **368**, 311 (2020).
- [98] T. Helbig, T. Hofmann, S. Imhof, M. Abdelghany, T. Kiessling, L. Molenkamp, C. Lee, A. Szameit, M. Greiter, and R. Thomale, Generalized bulk–boundary correspondence in non-Hermitian topoelectrical circuits, *Nat. Phys.* **16**, 747 (2020).
- [99] M. Brandenbourger, X. Locsin, E. Lerner, and C. Coulais, Non-reciprocal robotic metamaterials, *Nat.*

- Commun. **10**, 4608 (2019).
- [100] Y. Chen, X. Li, C. Scheibner, V. Vitelli, and G. Huang, Realization of active metamaterials with odd micropolar elasticity, Nat. Commun. **12**, 5935 (2021).
- [101] L. Zhang, Y. Yang, Y. Ge, Y.-J. Guan, Q. Chen, Q. Yan, F. Chen, R. Xi, Y. Li, D. Jia, *et al.*, Acoustic non-Hermitian skin effect from twisted winding topology, Nat. Commun. **12**, 6297 (2021).
- [102] L. S. Palacios, S. Tchoumakov, M. Guix, I. Pagonabarraga, S. Sánchez, and A. G. Grushin, Guided accumulation of active particles by topological design of a second-order skin effect, Nat. Commun. **12**, 4691 (2021).
- [103] C. Shang, S. Liu, R. Shao, P. Han, X. Zang, X. Zhang, K. N. Salama, W. Gao, C. H. Lee, R. Thomale, A. Manchon, S. Zhang, T. J. Cui, and U. Schwingenschlögl, Experimental Identification of the Second-Order Non-Hermitian Skin Effect with Physics-Graph-Informed Machine Learning, Adv. Sci. **9**, 2202922 (2022).
- [104] A. Altland and M. R. Zirnbauer, Nonstandard symmetry classes in mesoscopic normal-superconducting hybrid structures, Phys. Rev. B **55**, 1142 (1997).

# Supplemental Material for “Nonsymmorphic-Symmetry-Enforced Non-Hermitian Skin Effects”

Yutaro Tanaka,<sup>1</sup> Ryo Takahashi,<sup>2</sup> and Ryo Okugawa<sup>3</sup>

<sup>1</sup>*Department of Physics, Tokyo Institute of Technology,  
2-12-1 Ookayama, Meguro-ku, Tokyo 152-8551, Japan*

<sup>2</sup>*Advanced Institute for Materials Research (WPI-AIMR), Tohoku University, Sendai 980-8577, Japan*

<sup>3</sup>*Department of Applied Physics, Tokyo University of Science, Tokyo 125-8585, Japan*

## CONTENTS

Supplemental Material I. Tight-binding model in class AII <sup>†</sup>	2
Supplemental Material II. Review of doubled Hermitian Hamiltonians and winding numbers	2
A. Winding numbers for non-Hermitian Hamiltonians and doubled Hermitian Hamiltonians	2
B. Winding number and Chirality of Weyl points	3
Supplemental Material III. Symmetry conditions for non-Hermitian Hamiltonians	4
A. Crystal symmetries of doubled Hermitian Hamiltonians	4
B. Conditions for the screw symmetry	5
C. Details of the mechanism of symmetry-enforced NHSEs in class A	5
D. Model calculation in class A	7
Supplemental Material IV. Details of the mechanisms of symmetry-enforced NHSEs in time-reversal invariant classes	8
A. class AII	9
B. class AII <sup>†</sup>	9
C. Model calculation in class AII	11
D. class AI and class AI <sup>†</sup>	13
Supplemental Material V. Details of calculations of the 3D symmetry-enforced NHSE	14
References	15

### Supplemental Material I. TIGHT-BINDING MODEL IN CLASS AII<sup>†</sup>

We show the real-space Hamiltonian of the tight-binding model in class AII<sup>†</sup> in Eq. (5) in the main text. The Hamiltonian on a square lattice has the two degrees of freedom  $A$  and  $B$  in each unit cell, which is given by

$$\begin{aligned}
H_{2D} = & \alpha \sum_{\mathbf{R}} \sum_{\mathbf{r}_x=0, \mathbf{e}_x} (-1)^{\mathbf{r}_x \cdot \mathbf{e}_x} \left( |\mathbf{R} + \mathbf{r}_x + \mathbf{e}_y, A\rangle \langle \mathbf{R}, A| + |\mathbf{R} - \mathbf{r}_x - \mathbf{e}_y, B\rangle \langle \mathbf{R}, B| \right) \\
& + i\beta \sum_{\mathbf{R}} \sum_{\mathbf{r}_x=0, \mathbf{e}_x} \left( |\mathbf{R} + \mathbf{r}_x - \mathbf{e}_y, A\rangle \langle \mathbf{R}, A| + |\mathbf{R} - \mathbf{r}_x + \mathbf{e}_y, B\rangle \langle \mathbf{R}, B| \right) \\
& + \gamma \sum_{\mathbf{R}} \sum_{\mathbf{r}_x=0, \mathbf{e}_x} \left( -|\mathbf{R} + \mathbf{e}_x, A\rangle \langle \mathbf{R}, B| + |\mathbf{R} - \mathbf{e}_x, A\rangle \langle \mathbf{R}, B| + \text{h.c.} \right), \tag{S1}
\end{aligned}$$

where  $\mathbf{R} = (x, y)$  is the position of the unit cell, and  $\mathbf{e}_x$  and  $\mathbf{e}_y$  are the unit vectors in the  $x$  and  $y$  directions, respectively. Let us introduce the Fourier transformations  $|\mathbf{k}\rangle = \frac{1}{\sqrt{N}} \sum_{\mathbf{R}} e^{i\mathbf{k} \cdot \mathbf{R}} |\mathbf{R}\rangle$ , where  $N$  is the number of unit cells. By using the Fourier transformation under the periodic boundary condition (PBC), we obtain the Bloch Hamiltonian in Eq. (5) in the main text.

### Supplemental Material II. REVIEW OF DOUBLED HERMITIAN HAMILTONIANS AND WINDING NUMBERS

#### A. Winding numbers for non-Hermitian Hamiltonians and doubled Hermitian Hamiltonians

We briefly review the relationship between the NHSE and the band topology of a doubled Hermitian Hamiltonian. Throughout this work, we choose the convention for non-Hermitian Hamiltonians  $H(\mathbf{k})$  to satisfy  $H(\mathbf{k} + \mathbf{G}) = H(\mathbf{k})$ , as used for the Fourier transformation in the previous section.

We start with a winding number for the NHSE in two-dimensional (2D) and three-dimensional (3D) non-Hermitian systems, which is defined as [1]

$$W(E) = \frac{1}{2\pi i} \oint_l d\mathbf{k} \cdot \partial_{\mathbf{k}} \log \det[H(\mathbf{k}) - E], \tag{S2}$$

where  $l$  is a loop in the Brillouin zone, and  $E$  is a reference energy. If a winding number with a reference energy is nonzero in the system, a NHSE happens under an open boundary condition (OBC) [1]. On the other hand, it is unclear what OBC leads to the NHSE among the various OBCs. We can determine how to take an OBC to observe a NHSE by choosing a line in the Brillouin zone as  $l$ . For instance, let us introduce the following winding number

$$W_i(k_{\perp}, E) = \frac{1}{2\pi i} \int_0^{2\pi} dk_i \frac{\partial}{\partial k_i} \log \det[H(\mathbf{k}) - E], \tag{S3}$$

where  $k_{\perp}$  is the wave vector perpendicular to  $k_i$  ( $i = x, y, z$ ). If  $W(k_{\perp}, E)$  is nonzero, a NHSE happens under the OBC in the  $i$  direction and under the PBC in the other directions [2]. In this work, we investigate the winding number with  $E = 0$ .

Next, we see the band topology of doubled Hermitian Hamiltonians. A doubled Hermitian Hamiltonian  $\tilde{H}(\mathbf{k})$  can be obtained from a non-Hermitian Hamiltonian  $H(\mathbf{k})$  and is described as

$$\tilde{H}(\mathbf{k}) = \begin{pmatrix} & H(\mathbf{k}) \\ H^{\dagger}(\mathbf{k}) & \end{pmatrix}. \tag{S4}$$

The doubled Hermitian Hamiltonian has chiral symmetry  $\Gamma = \text{diag}(\mathbf{1}_N, -\mathbf{1}_N)$ , where  $N$  is the matrix size of  $H(\mathbf{k})$ . For the topological classification of the doubled Hermitian Hamiltonians, we introduce the  $Q$  matrix defined as [3]

$$Q(\mathbf{k}) = 1 - 2 \sum_{\mathcal{E}_{\alpha} < 0} |\Psi^{\alpha}(\mathbf{k})\rangle \langle \Psi^{\alpha}(\mathbf{k})|, \tag{S5}$$

where  $|\Psi^\alpha(\mathbf{k})\rangle$  is an eigenstate of the doubled Hermitian Hamiltonian with the energy  $\mathcal{E}_\alpha$ . When chiral symmetry is diagonal, the  $Q$  matrix is block off-diagonal, represented by

$$Q(\mathbf{k}) = \begin{pmatrix} 0 & q(\mathbf{k}) \\ q^\dagger(\mathbf{k}) & 0 \end{pmatrix}, \quad (\text{S6})$$

where  $q(\mathbf{k})$  is a unitary matrix. When only chiral symmetry is present, the Hamiltonians belong to class AIII [4]. The Hermitian Hamiltonians can be characterized by

$$\nu_i(k_\perp) = \frac{1}{2\pi i} \int_0^{2\pi} dk_i \frac{\partial}{\partial k_i} \log \det[q(\mathbf{k})], \quad (\text{S7})$$

which is also a winding number [3]. In high-dimensional systems, the winding number  $\nu_i(k_\perp)$  is used to characterize the topological gapless band structures [3, 5].

Hereafter we show that the winding number  $W_i(k_\perp)$  in the main text is equivalent to the winding number  $\nu(k_\perp)$ , according to Ref. [5]. Any doubled Hermitian Hamiltonian  $\tilde{H}(\mathbf{k})$  commutes with the  $Q$  matrix because

$$\begin{aligned} \tilde{H}(\mathbf{k})Q(\mathbf{k}) &= \tilde{H}(\mathbf{k}) - 2 \sum_{\mathcal{E}_\alpha < 0} \mathcal{E}_\alpha |\Psi^\alpha(\mathbf{k})\rangle \langle \Psi^\alpha(\mathbf{k})| \\ &= Q(\mathbf{k})\tilde{H}(\mathbf{k}). \end{aligned} \quad (\text{S8})$$

Because the commutation relation can be written on the basis of Eq. (S6) as

$$\begin{pmatrix} 0 & H(\mathbf{k}) \\ H^\dagger(\mathbf{k}) & 0 \end{pmatrix} \begin{pmatrix} 0 & q(\mathbf{k}) \\ q^\dagger(\mathbf{k}) & 0 \end{pmatrix} - \begin{pmatrix} 0 & q(\mathbf{k}) \\ q^\dagger(\mathbf{k}) & 0 \end{pmatrix} \begin{pmatrix} 0 & H(\mathbf{k}) \\ H^\dagger(\mathbf{k}) & 0 \end{pmatrix} = 0, \quad (\text{S9})$$

we obtain

$$H(\mathbf{k})q^\dagger(\mathbf{k}) = q(\mathbf{k})H^\dagger(\mathbf{k}). \quad (\text{S10})$$

Therefore, we have

$$\det[H(\mathbf{k})q^\dagger(\mathbf{k})] = \det[q(\mathbf{k})H^\dagger(\mathbf{k})] = \det[H(\mathbf{k})q^\dagger(\mathbf{k})]^*, \quad (\text{S11})$$

which indicates that  $\det[H(\mathbf{k})q^\dagger(\mathbf{k})]$  is real. It follows that

$$\int_0^{2\pi} dk_i \frac{\partial}{\partial k_i} \log \det[H(\mathbf{k})q^\dagger(\mathbf{k})] = 0, \quad (\text{S12})$$

because the integrand  $\log \det[H(\mathbf{k})q^\dagger(\mathbf{k})]$  is real and periodic in the Brillouin zone. Eventually, we obtain

$$\begin{aligned} \int_0^{2\pi} dk_i \frac{\partial}{\partial k_i} \log \det[H(\mathbf{k})] &= - \int_0^{2\pi} dk_i \frac{\partial}{\partial k_i} \log \det[q^\dagger(\mathbf{k})] \\ &= \int_0^{2\pi} dk_i \frac{\partial}{\partial k_i} \log \det[q(\mathbf{k})], \end{aligned} \quad (\text{S13})$$

where we have used  $\log \det q(\mathbf{k}) = -\log \det q^\dagger(\mathbf{k})$  because of the unitarity of  $q(\mathbf{k})$ . From this equation, it is clear that  $\nu_i(k_\perp)$  is the same as  $W_i(k_\perp)$ .

## B. Winding number and Chirality of Weyl points

Here we review a relationship between a winding number and 2D Weyl points. In the presence of chiral symmetry, a 2D Weyl point at zero energy can have a nonzero chirality related to the winding number. When a 2D Weyl point is located at  $\mathbf{k}_0$  in the Brillouin zone, the chirality is given by [5, 6]

$$\nu(\mathbf{k}_0) = \frac{1}{2\pi i} \oint_{U(\mathbf{k}_0)} d\mathbf{k} \cdot \partial_{\mathbf{k}} \log \det[q(\mathbf{k})], \quad (\text{S14})$$

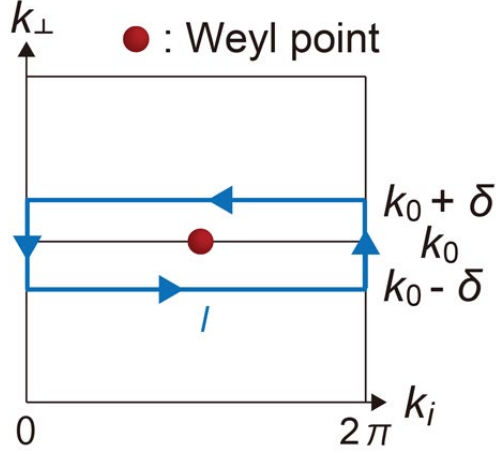


FIG. S1. An integral path  $l$  for the winding number encircling a Weyl point at  $k_{\perp} = k_0$ .

where  $l$  is a loop encircling the Weyl point. Moreover, when time-reversal symmetry  $\tilde{\mathcal{T}}$  is present, another Weyl point can appear at  $-\mathbf{k}_0$  if  $\mathbf{k}_0$  is not a time-reversal-invariant momentum. The chirality can be determined by whether the time-reversal and the chiral operators commute or anticommute. We write the relation as

$$\tilde{\mathcal{T}}\Gamma = c_{\tilde{\mathcal{T}}}\Gamma\tilde{\mathcal{T}}, \quad c_{\tilde{\mathcal{T}}} = \pm 1. \quad (\text{S15})$$

Then, winding numbers encircling each of the 2D Weyl points at  $\mathbf{k}_0$  and  $-\mathbf{k}_0$  are related via the relation [5]

$$\nu(-\mathbf{k}_0) = -c_{\tilde{\mathcal{T}}}\nu(\mathbf{k}_0). \quad (\text{S16})$$

We also show how the winding number in Eq. (S7) is related to the chirality. Let  $k_{\perp}$  be the wave vector perpendicular to  $k_i$ . We choose as  $l$  the integral path that encircles only one Weyl point at  $k_{\perp} = k_0$ , as shown in Fig. S1. Then, since  $\tilde{H}(\mathbf{k} + \mathbf{G}) = \tilde{H}(\mathbf{k})$  because of the gauge choice, the winding number is written as

$$\nu(\mathbf{k}_0) = \nu_i(k_0 - \delta) - \nu_i(k_0 + \delta), \quad (\text{S17})$$

where  $\delta$  is a real and positive value. Because the winding number  $\nu(\mathbf{k}_0)$  is nonzero, either  $\nu_i(k_0 + \delta)$  or  $\nu_i(k_0 - \delta)$  is nonzero. Thus, the Weyl point leads to the nonzero winding number  $W_i(k_{\perp})$  since  $\nu(k_{\perp}) = W_i(k_{\perp})$ .

We can generalize the idea to 3D systems. 3D chiral-symmetric systems can realize nodal lines due to band crossing instead of Weyl points because band degeneracy forms a gapless line in the 3D Brillouin zone [3]. The nodal line can be characterized by the same winding number in Eq. (S14). When we choose a loop linking with the nodal line as the integral path, the winding number is nonzero. By deforming the loop to a line in the same way as 2D, the system with the nodal line has a nonzero winding number in Eq. (1) in the main text.

### Supplemental Material III. SYMMETRY CONDITIONS FOR NON-HERMITIAN HAMILTONIANS

#### A. Crystal symmetries of doubled Hermitian Hamiltonians

First, we briefly explain how a doubled Hermitian Hamiltonian can obtain crystal symmetries from the non-Hermitian Hamiltonian. In this work, we use Seitz notation  $g = \{p_g | \mathbf{t}_g\}$  for a spatial transformation  $g$ , which transform a point  $\mathbf{r}$  as  $\mathbf{r} \rightarrow p_g \mathbf{r} + \mathbf{t}_g$ . Here  $p_g$  is an element of the point group, and  $\mathbf{t}_g$  represents a translation. When a doubled Hermitian Hamiltonian  $\tilde{H}(\mathbf{k})$  is symmetric under the symmetry operation  $g$ ,  $\tilde{U}_g^{\mathbf{k}} \tilde{H}(\mathbf{k}) (\tilde{U}_g^{\mathbf{k}})^{-1} = \tilde{H}(p_g \mathbf{k})$ , where  $\tilde{U}_g^{\mathbf{k}}$  is a symmetry representation of  $g$ . Moreover, since  $\tilde{H}(\mathbf{k})$  has chiral symmetry  $\Gamma = \text{diag}(\mathbf{1}_N, -\mathbf{1}_N)$ , we specify a relation between  $\tilde{U}_g^{\mathbf{k}}$  and  $\Gamma$  by using a projective factor  $c_g$ , which is defined as [7]

$$\tilde{U}_g^{\mathbf{k}} \Gamma = c_g \Gamma \tilde{U}_g^{\mathbf{k}}. \quad (\text{S18})$$

Because  $\Gamma^2 = 1$ , we obtain  $\tilde{U}_g^{\mathbf{k}}\Gamma = c_g^2\tilde{U}_g^{\mathbf{k}}\Gamma$ , which leads to  $c_g = \pm 1$ . Therefore, symmetry representations commute or anticommute with  $\Gamma$ . Indeed, crystal symmetries can be represented by [7]

$$\tilde{U}_g^{\mathbf{k}} = \begin{cases} \begin{pmatrix} A_g^{\mathbf{k}} & \\ & B_g^{\mathbf{k}} \end{pmatrix} & (c_g = 1), \\ \begin{pmatrix} & B_g^{\mathbf{k}} \\ A_g^{\mathbf{k}} & \end{pmatrix} & (c_g = -1), \end{cases} \quad (\text{S19})$$

where  $A_g^{\mathbf{k}}$  and  $B_g^{\mathbf{k}}$  are unitary matrices that are periodic in the Brillouin zone. If a doubled Hermitian Hamiltonian has crystal symmetry represented by  $\tilde{U}_g^{\mathbf{k}}$  in Eq. (S19), we can see that a non-Hermitian Hamiltonian needs to satisfy the symmetry relation given by

$$A_g^{\mathbf{k}}H(\mathbf{k}) = \begin{cases} H(p_g\mathbf{k})B_g^{\mathbf{k}} & (c_g = 1), \\ H^\dagger(p_g\mathbf{k})B_g^{\mathbf{k}} & (c_g = -1). \end{cases} \quad (\text{S20})$$

It is noted that Eqs. (S19) and (S20) hold true even if time-reversal symmetry is present.

The projective factors relate the symmetry eigenvalues of two eigenstates connected by chiral symmetry. Since doubled Hermitian Hamiltonians have chiral symmetry  $\Gamma$ , an eigenstate  $|\Psi(\mathbf{k})\rangle$  with the energy  $\mathcal{E}$  appears with the chiral partner  $\Gamma|\Psi(\mathbf{k})\rangle$  with  $-\mathcal{E}$ . The eigenstates have symmetry eigenvalues at the high-symmetry point, which is invariant under  $P_g$  on the high-symmetry points. When  $\tilde{U}_g^{\mathbf{k}}|\Psi(\mathbf{k})\rangle = u_g|\Psi(\mathbf{k})\rangle$  where  $u_g$  is an eigenvalue of the crystal symmetry  $g$ , the chiral partner satisfies  $\tilde{U}_g^{\mathbf{k}}\Gamma|\Psi(\mathbf{k})\rangle = c_g u_g \Gamma|\Psi(\mathbf{k})\rangle$ . Hence, if  $c_g = +1(-1)$ , the symmetry eigenvalues of  $|\Psi(\mathbf{k})\rangle$  and  $\Gamma|\Psi(\mathbf{k})\rangle$  have the same (opposite) signs.

## B. Conditions for the screw symmetry

Next, we apply the above conditions to the screw symmetry  $g = \{C_{2x}|\hat{\mathbf{x}}/2\}$ , represented by

$$\tilde{U}_g^{\mathbf{k}}\tilde{H}(\mathbf{k})(\tilde{U}_g^{\mathbf{k}})^{-1} = \tilde{H}(C_{2x}\mathbf{k}), \quad (\text{S21})$$

where  $\hat{\mathbf{x}}$  is a primitive vector in the  $x$  direction,  $C_{2x}\mathbf{k} = (k_x, -k_y)$ , and  $\tilde{U}_g^{\mathbf{k}}$  is a representation matrix of the screw symmetry. Because  $\{C_{2x}|\hat{\mathbf{x}}/2\}^2 = \{C_{2x}^2|\hat{\mathbf{x}}\}$ , it follows that  $\tilde{U}_g^{C_{2x}\mathbf{k}}\tilde{U}_g^{\mathbf{k}} = e^{-ik_x}(-e^{-ik_x})$  for  $C_{2x}^2 = 1(-1)$ . Therefore, we obtain the following equations:

$$c_s A_g^{\mathbf{k}} = (c_s e^{ik_x} A_g^{C_{2x}\mathbf{k}})^\dagger, \quad c_s B_g^{\mathbf{k}} = (c_s e^{ik_x} B_g^{C_{2x}\mathbf{k}})^\dagger \quad (c_g = 1), \quad (\text{S22})$$

$$c_s B_g^{\mathbf{k}} = (c_s e^{ik_x} A_g^{C_{2x}\mathbf{k}})^\dagger \quad (c_g = -1), \quad (\text{S23})$$

where  $c_s = 1(i)$  for  $C_{2x}^2 = 1(-1)$ , and  $A_g^{\mathbf{k}}$  and  $B_g^{\mathbf{k}}$  are unitary matrices in Eq. (S19). By combining Eq. (S20) with Eq. (S23), we can obtain

$$A_g^{\mathbf{k}}H(\mathbf{k}) = H(C_{2x}\mathbf{k})B_g^{\mathbf{k}} \quad (c_g = 1), \quad (\text{S24})$$

$$c_s A_g^{\mathbf{k}}H(\mathbf{k}) = \left(c_s e^{ik_x} A_g^{C_{2x}\mathbf{k}} H(C_{2x}\mathbf{k})\right)^\dagger \quad (c_g = -1). \quad (\text{S25})$$

In this work, we show that symmetry-enforced NHSEs happen when  $c_g = -1$ . By using a unitary matrix  $U_g^{\mathbf{k}} := c_s e^{i\frac{k_x}{2}} A_g^{\mathbf{k}}$ , we can rewrite Eq. (S25) as Eq. (2) in the main text.

## C. Details of the mechanism of symmetry-enforced NHSEs in class A

We henceforth show that screw symmetry with  $c_g = -1$  yields the nonsymmorphic symmetry-enforced NHSE. We assume that the matrix size of  $H(\mathbf{k})$  is  $2M + 1$  with a nonnegative integer  $M$ . When  $H(\mathbf{k})$  satisfies Eq. (S25), the doubled Hermitian Hamiltonian  $\tilde{H}(\mathbf{k})$  has the screw rotation symmetry. Eigenstates of  $\tilde{H}(\mathbf{k})$  can be labeled by the symmetry eigenvalues  $\pm c_s e^{-i\frac{k_x}{2}}$  on the screw-invariant lines. By replacing  $k_x$  with  $k_x + 2\pi$ , the eigenvalues change

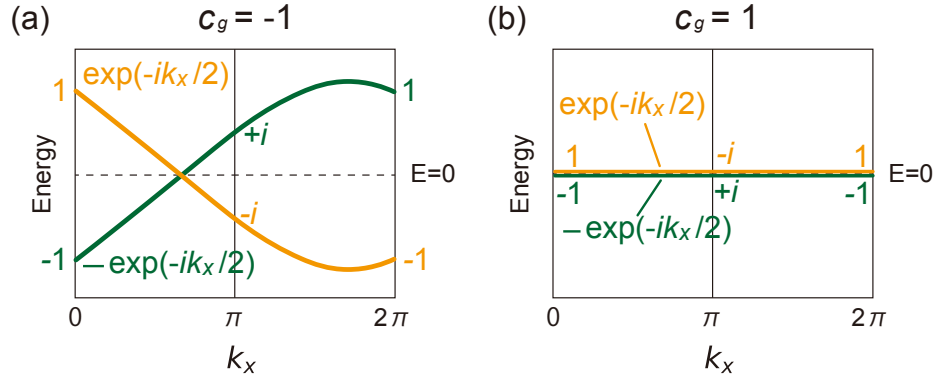


FIG. S2. Weyl point and gapless line in a 2D doubled Hermitian Hamiltonian with screw symmetry in class AIII. The yellow (green) lines represent energy eigenvalues with the screw symmetry eigenvalue  $+e^{-ik_x/2}$  ( $-e^{ik_x/2}$ ). (a) and (b) show energy bands along a screw-invariant line in the cases where the chiral and the screw symmetries satisfy the anticommutation relation ( $c_g = -1$ ) and commutation relation ( $c_g = 1$ ), respectively.

from  $\pm c_s e^{-i\frac{k_x}{2}}$  to  $\mp c_s e^{-i\frac{k_x}{2}}$ . Therefore, pairs of bands with opposite eigenvalues must intersect an odd number of times [8] from  $k_x = 0$  to  $k_x = 2\pi$  on the screw-invariant line, which enforces 2D Weyl points [9].

We consider the effect of chiral symmetry on the band structures of the doubled Hermitian Hamiltonian. Because of the chiral symmetry  $\Gamma$ , an eigenstate with the energy  $\mathcal{E}$  appears with an eigenstate with  $-\mathcal{E}$  in pairs. When  $\Gamma$  and  $\tilde{U}_g^k$  satisfy anticommutation relation (i.e.  $c_g = -1$ ), a pair of the eigenstates has the screw eigenvalues with opposite signs [Fig. S2(a)]. The two eigenstates with opposite screw symmetry eigenvalues intersect an odd number of times along the screw-invariant line. The crossing points are 2D Weyl points. By assumption about the matrix size, the Weyl points appear at zero energy, which gives a nonzero winding number.

In contrast, when  $c_g = 1$ , the pair of states with the energy  $\mathcal{E}$  and  $-\mathcal{E}$  have the same screw symmetry eigenvalues [Fig. S2(b)]. Therefore, the screw symmetry with  $c_g = 1$  leads to gap-closing lines at zero energy. Hence, the 2D Weyl points do not appear in this case, and we do not consider this case in our paper.

When the doubled Hermitian Hamiltonian  $\tilde{H}(\mathbf{k})$  has a nonzero winding number, the non-Hermitian Hamiltonian  $H(\mathbf{k})$  also has nonzero  $W_i(k_\perp)$ , as discussed above. Thus, corresponding to the 2D Weyl points enforced by the screw symmetry, the non-Hermitian Hamiltonian  $H(\mathbf{k})$  has a nonzero winding number [Fig. S3]. Also, because the positions of the Weyl points are fixed on the screw-invariant lines ( $k_y = 0, \pi$ ), there is always at least one direction where the

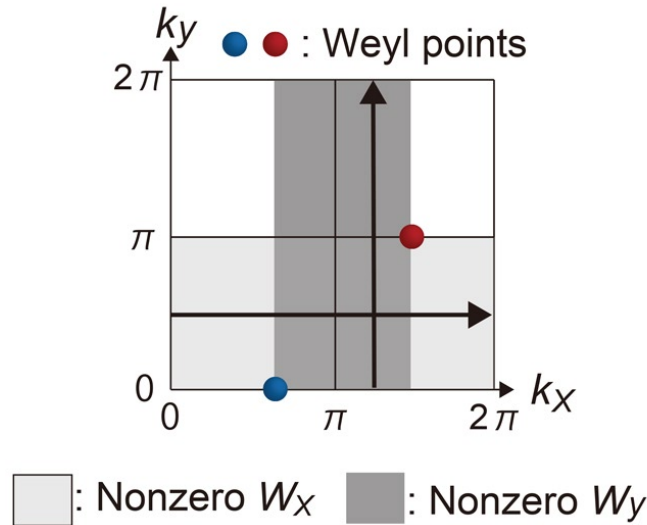


FIG. S3. Weyl points and regions with the nonzero winding number  $W_i(k_\perp)$  ( $i = x, y$ ). The arrows indicate the direction of the integration of  $W_i(k_\perp)$ . The red and the blue points are Weyl points, and the color difference represents their opposite chirality.

winding number is nonzero regardless of the positions of the Weyl points. As a result, a NHSE along some direction is also enforced by the screw symmetry of  $\hat{H}(\mathbf{k})$ . Namely, because a winding number is necessarily nonzero in the Brillouin zone thanks to the symmetry-enforced Weyl points, the NHSE is robust as long as  $H(\mathbf{k})$  satisfies Eq. (S25).

Intriguingly, we can find anisotropy of winding numbers for the symmetry-enforced NHSE in class A since Weyl points are enforced to appear on the screw-invariant lines. When two Weyl points are located on the same  $k_x$  line, there is no region where  $W_y(k_x)$  is nonzero. On the other hand, we can always find a path for a nonzero  $W_x(k_y)$  in the Brillouin zone, as shown in Fig. S3. Thus, the symmetry-enforced NHSE under the OBC in the  $x$  direction is more robust than that under the OBC in the  $y$  direction.

#### D. Model calculation in class A

To demonstrate a nonsymmorphic-symmetry-enforced NHSE in class A, we introduce a tight-binding model. The Hamiltonian on the square lattice is given by

$$H_{2D}^A = \sum_{\mathbf{R}} \sum_{\mathbf{r}_x = -\mathbf{e}_x, 2\mathbf{e}_x} \left( t_1 |\mathbf{R} + \mathbf{r}_x\rangle \langle \mathbf{R}| + t_2 |\mathbf{R} + \mathbf{r}_x + \mathbf{e}_y\rangle \langle \mathbf{R}| + t_3 |\mathbf{R} + \mathbf{r}_x\rangle \langle \mathbf{R} + \mathbf{e}_y| \right) + \sum_{\mathbf{R}} \sum_{\mathbf{r}_x = 0, \mathbf{e}_x} \left( it_4 (-1)^{\mathbf{r}_x \cdot \mathbf{e}_x} |\mathbf{R} + \mathbf{r}_x + \mathbf{e}_y\rangle \langle \mathbf{R}| + it_5 (-1)^{\mathbf{r}_x \cdot \mathbf{e}_x} |\mathbf{R} + \mathbf{r}_x\rangle \langle \mathbf{R} + \mathbf{e}_y| \right), \quad (\text{S26})$$

where  $\mathbf{R} = (x, y)$  is the position of the unit cell, and  $\mathbf{e}_x$  and  $\mathbf{e}_y$  are the unit vectors in the  $x$  and  $y$  directions, respectively. Let us introduce the Fourier transformations  $|\mathbf{k}\rangle = \frac{1}{\sqrt{N}} \sum_{\mathbf{R}} e^{i\mathbf{k} \cdot \mathbf{R}} |\mathbf{R}\rangle$ , where  $N$  is the number of unit cells. By using the Fourier transformation under the PBC, we obtain the Bloch Hamiltonian

$$H_{2D}^A(\mathbf{k}) = (e^{ik_x} + e^{-2ik_x})(t_1 + t_2 e^{-ik_y} + t_3 e^{ik_y}) + i(1 - e^{-ik_x})(t_4 e^{-ik_y} + t_5 e^{ik_y}). \quad (\text{S27})$$

The Hamiltonian  $H_{2D}^A(\mathbf{k})$  satisfies the condition in Eq. (S25) with  $c_s = 1$  and  $A_g^k = 1$ . Figure S4(a) shows energy spectra of  $H_{2D}^A(\mathbf{k})$  on the  $k_x = \pi$  line under both the full PBC and the OBC in the  $y$  direction. Figure S4(b) shows spatial distributions for all the eigenstates, and we can see that they are localized at the right edge. These results

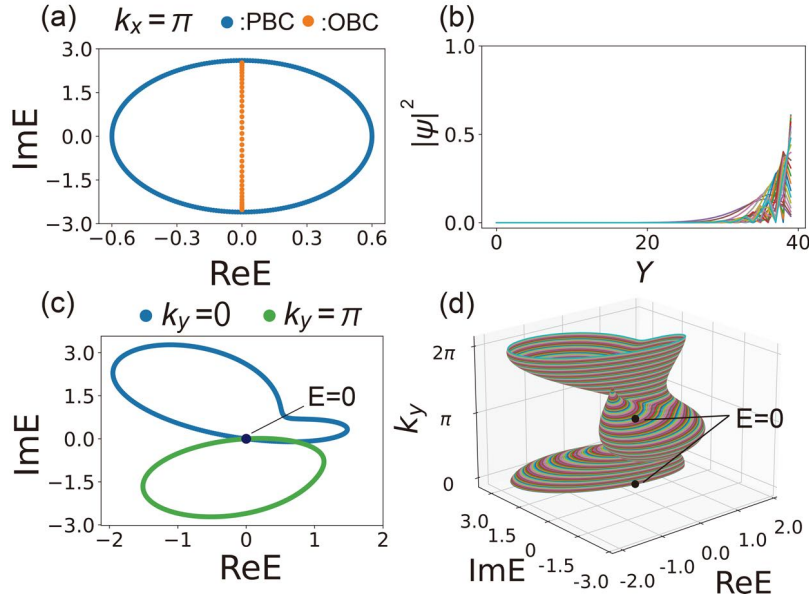


FIG. S4. Energy spectra and eigenstates of  $H_{2D}^A(\mathbf{k})$  with the parameters  $t_1 = 0.4$ ,  $t_2 = 0.1$ ,  $t_3 = 0.1$ ,  $t_4 = 0.8$ , and  $t_5 = 0.5$ . We take the PBC in the  $x$  direction for all the calculations. (a) The energy spectra on the  $k_x = \pi$  line under the PBC and the OBC in the  $y$  direction. (b) The spatial distributions of all the right eigenstates  $\psi_n$  on the  $k_x = \pi$  line. (c) The energy spectra on the  $k_y = 0$  and  $k_y = \pi$  lines under the full PBC. (d) The energy spectra in  $E$ - $k_y$  space.

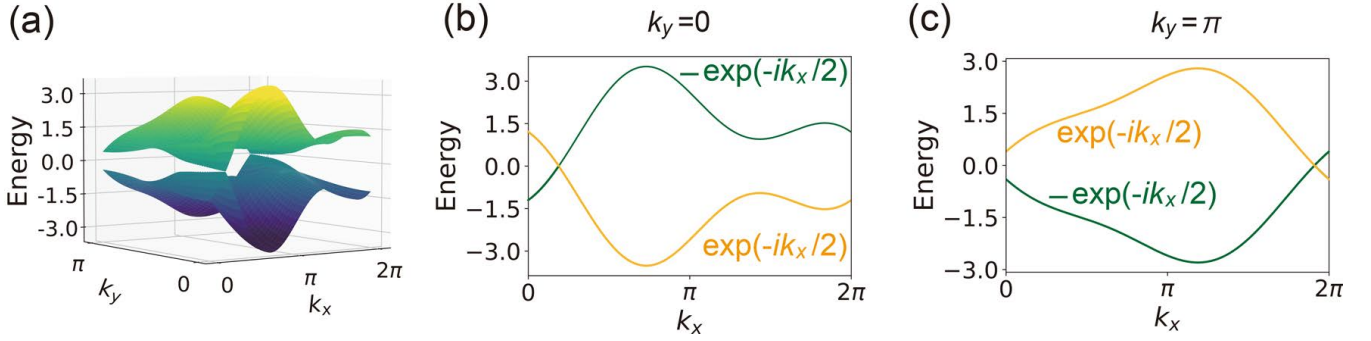


FIG. S5. (a) The band structures of  $\tilde{H}_{2D}^{\text{AIII}}(\mathbf{k})$ . (b,c) The energy bands of  $\tilde{H}_{2D}^{\text{AIII}}(\mathbf{k})$  along the screw-invariant line (b) at  $k_y = 0$  and (c) at  $k_y = \pi$ . Here we choose the parameters  $t_1 = 0.4$ ,  $t_2 = 0.1$ ,  $t_3 = 0.1$ ,  $t_4 = 0.8$ , and  $t_5 = 0.5$ .

indicate that a NHSE occurs in the model. Moreover, the point gap closes at  $E = 0$  on the  $k_y = 0$  and  $k_y = \pi$  lines under the full PBC [Figs. S4(c) and S4(d)].

Next, we investigate a doubled Hermitian Hamiltonian  $\tilde{H}_{2D}^{\text{AIII}}(\mathbf{k})$  obtained from  $H_{2D}^{\text{A}}(\mathbf{k})$ . The doubled Hermitian Hamiltonian can be written as

$$\tilde{H}_{2D}^{\text{AIII}}(\mathbf{k}) = \begin{pmatrix} H_{2D}^{\text{A}}(\mathbf{k}) & \\ & H_{2D}^{\text{A}}(\mathbf{k})^\dagger \end{pmatrix} \quad (\text{S28})$$

$$= f_x(\mathbf{k})\sigma_x + f_y(\mathbf{k})\sigma_y \quad (\text{S29})$$

where  $\sigma_i$  ( $i = x, y, z$ ) are Pauli matrices, and

$$\begin{aligned} f_x(\mathbf{k}) &= (\cos k_x + \cos 2k_x)(t_1 + t_2 \cos k_y + t_3 \cos k_y) + (-\sin k_x + \sin 2k_x)(-t_2 \sin k_y + t_3 \sin k_y) \\ &\quad + (t_4 - t_5)(1 - \cos k_x) \sin k_y - (t_4 + t_5) \sin k_x \cos k_y, \\ f_y(\mathbf{k}) &= -(\cos k_x + \cos 2k_x)(-t_2 \sin k_y + t_3 \sin k_y) - (\sin k_x - \sin 2k_x)(t_1 + t_2 \cos k_y + t_3 \cos k_y) \\ &\quad - (t_4 + t_5)(1 - \cos k_x) \cos k_y + (-t_4 + t_5) \sin k_x \sin k_y. \end{aligned} \quad (\text{S30})$$

The doubled Hermitian Hamiltonian has chiral symmetry represented by  $\Gamma \tilde{H}_{2D}^{\text{AIII}}(\mathbf{k}) \Gamma^{-1} = -\tilde{H}_{2D}^{\text{AIII}}(\mathbf{k})$  with  $\Gamma = \sigma_z$ . The screw  $g = \{C_{2x}|\hat{\mathbf{x}}/2\}$  symmetry of the doubled Hermitian Hamiltonian is represented by

$$\tilde{U}_g^{\mathbf{k}} \tilde{H}_{2D}^{\text{AIII}}(\mathbf{k}) (\tilde{U}_g^{\mathbf{k}})^{-1} = \tilde{H}_{2D}^{\text{AIII}}(C_{2x}\mathbf{k}), \quad \tilde{U}_g^{\mathbf{k}} = \begin{pmatrix} e^{-ik_x} & \\ & 1 \end{pmatrix}. \quad (\text{S31})$$

Because  $\tilde{U}_g^{C_{2x}\mathbf{k}} \tilde{U}_g^{\mathbf{k}} = e^{-ik_x}$  in the model, the screw symmetry eigenvalues are  $\pm e^{-ik_x/2}$ . Moreover,  $\tilde{U}_g^{\mathbf{k}}$  and  $\Gamma$  satisfy the anticommutation relation  $\tilde{U}_g^{\mathbf{k}} \Gamma = -\Gamma \tilde{U}_g^{\mathbf{k}}$ , which corresponds to  $c_g = -1$ .

Figure S5(a) shows the band structure of the doubled Hermitian Hamiltonian  $\tilde{H}_{2D}^{\text{AIII}}(\mathbf{k})$ , where we can find two Weyl points at zero energy. Figures S5(b) and S5(c) show the band structures along the screw-invariant line at  $k_y = 0$  and  $k_y = \pi$ . We can see that the two eigenstates with screw eigenvalues with opposite signs switch, leading to the Weyl points. Since a winding number is nonzero between the Weyl points, the NHSE necessarily occurs.

#### Supplemental Material IV. DETAILS OF THE MECHANISMS OF SYMMETRY-ENFORCED NHSES IN TIME-REVERSAL INVARIANT CLASSES

In this section, we study symmetry-enforced NHSEs in time-reversal invariant classes. We clarify the relationship between NHSEs and 2D Weyl points enforced by the screw symmetry when the screw operator commutes with the time-reversal operator. In particular, we focus on the case with  $c_g = -1$  in Eq. (S25) to enforce Weyl points similarly to class A.

### A. class AII

Next, we discuss symmetry-enforced NHSEs in class AII [10]. Let us assume that a non-Hermitian Hamiltonian  $H(\mathbf{k})$  in class AII satisfies Eq. (S25). The non-Hermitian Hamiltonian  $H(\mathbf{k})$  has time-reversal symmetry

$$\mathcal{T}H^*(\mathbf{k})\mathcal{T}^{-1}=H(-\mathbf{k}), \quad \mathcal{T}\mathcal{T}^*=-1, \quad (\text{S32})$$

where  $\mathcal{T}$  is a unitary matrix. The doubled Hermitian Hamiltonian  $\tilde{H}(\mathbf{k})$  has time-reversal symmetry given by

$$\tilde{\mathcal{T}}\tilde{H}(\mathbf{k})\tilde{\mathcal{T}}^{-1}=\tilde{H}(-\mathbf{k}), \quad \tilde{\mathcal{T}}=\begin{pmatrix} \mathcal{T} & \\ & \mathcal{T} \end{pmatrix}K, \quad \tilde{\mathcal{T}}^2=-1. \quad (\text{S33})$$

The doubled Hermitian Hamiltonian  $\tilde{H}(\mathbf{k})$  has particle-hole symmetry given by  $\tilde{\mathcal{P}}=\tilde{\mathcal{T}}^{-1}\Gamma$ , and therefore  $\tilde{\mathcal{P}}^2=-1$  due to  $\Gamma\tilde{\mathcal{T}}=\tilde{\mathcal{T}}\Gamma$  (i.e.  $c_{\tilde{\mathcal{T}}}=1$ ). Thus,  $\tilde{H}(\mathbf{k})$  belongs to class CII. We also impose the condition that  $g=\{C_{2x}|\hat{x}/2\}$  and  $\tilde{\mathcal{T}}$  commute in order to specify their relation. Then, because  $\tilde{\mathcal{T}}\tilde{U}_g^{\mathbf{k}}=\tilde{U}_g^{-\mathbf{k}}\tilde{\mathcal{T}}$ , we obtain

$$\mathcal{T}(A_g^{\mathbf{k}})^*=A_g^{-\mathbf{k}}\mathcal{T}, \quad (\text{S34})$$

$$\mathcal{T}(B_g^{\mathbf{k}})^*=B_g^{-\mathbf{k}}\mathcal{T}. \quad (\text{S35})$$

By using the unitary matrix  $U_g^{\mathbf{k}}=ie^{i\frac{k_x}{2}}A_g^{\mathbf{k}}$ , we can rewrite Eq. (S34) as

$$\mathcal{T}(U_g^{\mathbf{k}})^*=-U_g^{-\mathbf{k}}\mathcal{T}. \quad (\text{S36})$$

In this work, we consider the case for  $c_s=i$  since  $\tilde{\mathcal{T}}^2=-1$  corresponds to spinful systems with  $C_{2x}^2=-1$ . We investigate energy bands of the doubled Hermitian Hamiltonian. Even if screw symmetry coexists with time-reversal symmetry with  $\tilde{\mathcal{T}}^2=-1$ , 2D Weyl points appear on the screw-invariant lines in the  $k$  space [9, 11]. Let us assume that a non-Hermitian Hamiltonian has a matrix size of  $4M+2$ . We show that the doubled Hermitian Hamiltonian has 2D Weyl points at zero energy if  $c_g=-1$ , although chiral symmetry is also present. The eigenstates on the screw-invariant lines ( $k_y=0, \pi$ ) are labeled by the screw rotation eigenvalues  $\pm ie^{-i\frac{k_x}{2}}$ . Because of the time-reversal symmetry, while Kramers pairs at  $k_x=0$  have opposite screw rotation eigenvalues  $\pm i$ , Kramers pairs at  $k_x=\pi$  have the same eigenvalues [Fig. S6(a)]. Moreover, because the chiral operator anticommutes with the screw operator, a pair of eigenstates with the energy  $\mathcal{E}$  and  $-\mathcal{E}$  has screw eigenvalues with the opposite signs. Since the eigenvalues must exchange on the line, the eigenstates with these symmetry eigenvalues enforce Weyl points on the screw-invariant line. Because the number of bands of the doubled Hermitian Hamiltonian is  $8M+4$  by assumption, the chiral symmetry fixes the 2D Weyl points at zero energy. Similarly to class A, the non-Hermitian Hamiltonian  $H(\mathbf{k})$  has a nonzero winding number  $W_i(k_{\perp})$  between the two 2D Weyl points in the doubled Hermitian Hamiltonian  $\tilde{H}(\mathbf{k})$ .

Moreover, we discuss the nonzero winding numbers due to the positions of the Weyl points with  $c_g=-1$  in the Brillouin zone. By using Eq. (S16) with  $c_{\tilde{\mathcal{T}}}=1$ , we find that the time-reversal pair of Weyl points on the screw-invariant line has opposite chirality. Therefore, two types of positions of the 2D Weyl points can be realized, as shown in Fig. S6(c). Because of these positions of the Weyl points, the winding number  $W_x(k_y)$  is zero in Fig. S6(c). In contrast, the winding number  $W_y(k_x)$  can be nonzero in the regions in this case.

Here, we comment on the case with  $c_g=1$ , where  $\Gamma$  and  $\tilde{U}_g^{\mathbf{k}}$  commute. In this case, a pair of eigenstates at energy  $\mathcal{E}$  and  $-\mathcal{E}$  have the same eigenvalues of the screw symmetry. On the other hand, the time-reversal symmetry gives rise to Kramer's degeneracy of two states with the same screw eigenvalues. Therefore, the screw symmetry with  $c_g=1$  leads to a four-fold degeneracy at  $k_x=\pi$  [Fig. S6(b)], and this case is beyond our scope.

### B. class AII<sup>†</sup>

Finally, we investigate symmetry-enforced NHSEs in class AII<sup>†</sup> [10]. The non-Hermitian Hamiltonian  $H(\mathbf{k})$  has time-reversal symmetry defined as

$$\mathcal{T}H^T(\mathbf{k})\mathcal{T}^{-1}=H(-\mathbf{k}), \quad \mathcal{T}\mathcal{T}^*=-1, \quad (\text{S37})$$

where  $\mathcal{T}$  is a unitary matrix [10]. The doubled Hermitian Hamiltonian  $\tilde{H}(\mathbf{k})$  can obtain time-reversal symmetry given by

$$\tilde{\mathcal{T}}\tilde{H}(\mathbf{k})\tilde{\mathcal{T}}^{-1}=\tilde{H}(-\mathbf{k}), \quad \tilde{\mathcal{T}}=\begin{pmatrix} & \mathcal{T} \\ \mathcal{T} & \end{pmatrix}K, \quad \tilde{\mathcal{T}}^2=-1. \quad (\text{S38})$$

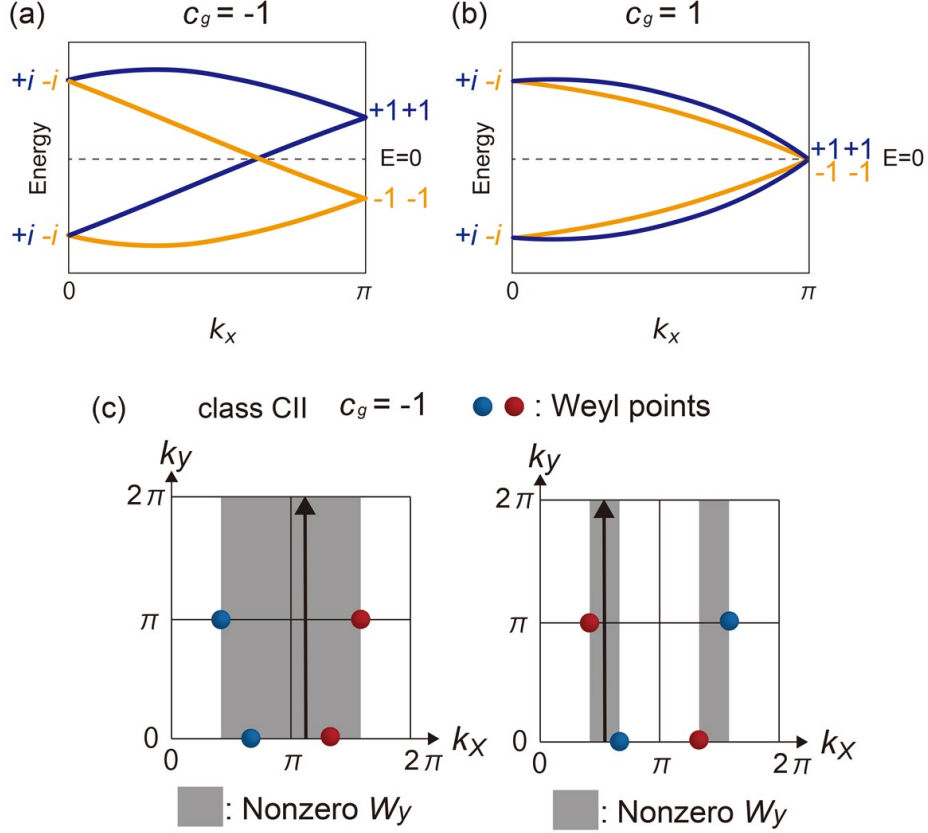


FIG. S6. (a), (b) Nonsymmorphic-symmetry enforced Weyl and fourfold-degenerate points in a 2D doubled Hermitian Hamiltonian in symmetry class CII. Energy spectra along a screw-symmetry line with  $\Gamma$  and  $\tilde{U}_g^k$  satisfying (a) anticommutation relation and (b) commutation relation. (c) Illustrative examples of the positions of the Weyl points with  $c_g = -1$  in class CII and the regions with the nonzero winding number  $W_y(k_x)$  in the Brillouin zone. When a non-Hermitian Hamiltonian belongs to class AII, the class of the doubled Hermitian Hamiltonian is CII. The arrows indicate the direction of integration of  $W_y(k_x)$ . The colors (red and blue) of the points represent the opposite chirality of the Weyl points. Here we assume  $W_y(0) = 0$ , otherwise the nonzero  $W_y(k_x)$  regions and the zero  $W_y(k_x)$  regions are interchanged.

The symmetry class of  $\tilde{H}(\mathbf{k})$  is class DIII [4] because  $\tilde{H}(\mathbf{k})$  has particle-hole symmetry that satisfies  $\tilde{\mathcal{P}}^2 = 1$  owing to  $\Gamma\tilde{\mathcal{T}} = -\tilde{\mathcal{T}}\Gamma$ . Therefore, we have  $c_{\tilde{\mathcal{T}}} = -1$ . We also obtain  $\tilde{\mathcal{T}}\tilde{U}_g^k = \tilde{U}_g^{-k}\tilde{\mathcal{T}}$  by imposing the commutation relation on  $\{C_{2x}|\hat{x}/2\}$  and  $\tilde{\mathcal{T}}$ . Therefore, we have

$$\mathcal{T}(A_g^k)^* = B_g^{-k}\mathcal{T}. \quad (\text{S39})$$

Moreover, we choose  $c_s = i$  because  $\tilde{\mathcal{T}}^2 = -1$ . Hence, we obtain

$$\mathcal{T}(A_g^k)^* = -e^{ik_x}(A_g^{-C_{2x}k})^{-1}\mathcal{T}. \quad (\text{S40})$$

By using the unitary matrix  $U_g^k = ie^{i\frac{k_x}{2}}A_g^k$ , we get

$$\mathcal{T}(U_g^k)^* = -(U_g^{-C_{2x}k})^\dagger\mathcal{T}. \quad (\text{S41})$$

Let us assume that the matrix size of  $H(\mathbf{k})$  is  $4M + 2$ , and that  $H(\mathbf{k})$  satisfies Eq. (S25). Similarly to class AII, the doubled Hermitian Hamiltonian  $\tilde{H}(\mathbf{k})$  has 2D Weyl points on the screw-invariant line at  $k_y = 0$  and  $k_y = \pi$  [Fig. S6(a)]. Meanwhile, because  $c_{\tilde{\mathcal{T}}} = -1$ , we find that a time-reversal pair of the Weyl points on the screw-invariant line has the same chirality [Fig. S7]. Therefore, the nonzero winding numbers are different from those in class AII, as shown in Fig. S7. Furthermore, we can find anisotropy of the winding numbers in the same way as class A because we cannot annihilate the Weyl points on the screw-invariant lines. As a result, the NHSE under the OBC in the  $x$  direction is more robust than that under the OBC in the  $y$  direction.

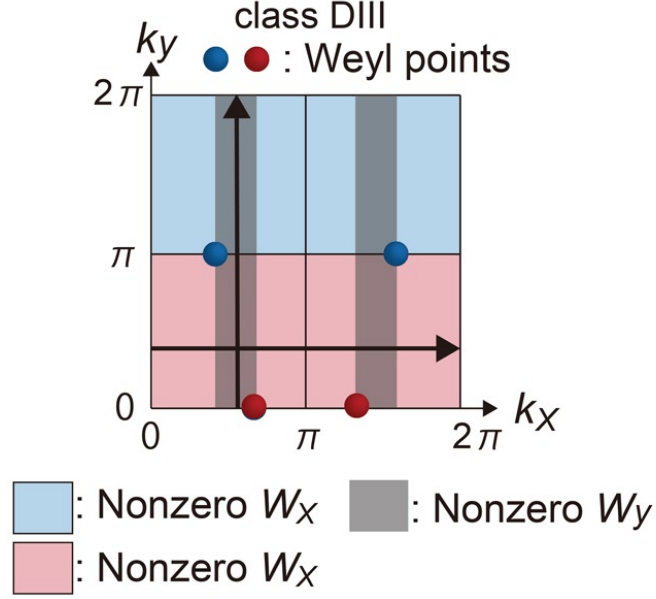


FIG. S7. An illustrative example of the positions of the Weyl points in class DIII with  $c_g = -1$  and the regions with the nonzero winding number in the Brillouin zone. When a non-Hermitian Hamiltonian belongs to class AII<sup>†</sup>, the class of the doubled Hermitian Hamiltonian is DIII. The arrows indicate the direction of integration of  $W_i(k_\perp)$ . The colors (red and blue) of the points represent the opposite chirality of the Weyl points. The red and blue colors of the nonzero  $W_x(k_y)$  regions indicate the opposite sign of the winding number:  $W_x(k_y) = -W_x(-k_y)$ .

### C. Model calculation in class AII

To show a symmetry-enforced NHSE in class AII, let us introduce a 2D tight-binding model on a square lattice with the two degrees of freedom  $A$  and  $B$  in each unit cell. This model is given by

$$H_{2D}^{\text{AII}} = H_{2D}^{\text{AII}(1)} + H_{2D}^{\text{AII}(2)} + H_{2D}^{\text{AII}(3)}, \quad (\text{S42})$$

$$\begin{aligned}
H_{2D}^{\text{AII}(1)} = & -it \sum_{\mathbf{R}} \sum_{\mathbf{r}=0, \mathbf{e}_x, \mathbf{e}_y, \mathbf{e}_x+\mathbf{e}_y} (-1)^{\mathbf{r} \cdot (\mathbf{e}_x + \mathbf{e}_y)} \left( |\mathbf{R} + \mathbf{r}, B\rangle \langle \mathbf{R}, A| + |\mathbf{R} + \mathbf{r}, A\rangle |\mathbf{R}, B\rangle \right) \\
& - 0.5it \sum_{\mathbf{R}} \sum_{\mathbf{r}=0, \mathbf{e}_x} (-1)^{\mathbf{r} \cdot \mathbf{e}_x} \left( |\mathbf{R} + \mathbf{r} - \mathbf{e}_y, B\rangle \langle \mathbf{R}, A| + |\mathbf{R} + \mathbf{r} - \mathbf{e}_y, A\rangle \langle \mathbf{R}, B| \right), \quad (\text{S43})
\end{aligned}$$

$$\begin{aligned}
H_{2D}^{\text{AII}(2)} = & v \sum_{\mathbf{R}} \sum_{\mathbf{r}_x=0, \mathbf{e}_x} \left( -2 |\mathbf{R} + \mathbf{r}_x, A\rangle \langle \mathbf{R}, B| + 2 |\mathbf{R} + \mathbf{r}_x, B\rangle \langle \mathbf{R}, A| \right. \\
& + |\mathbf{R} + \mathbf{r}_x - \mathbf{e}_y, A\rangle \langle \mathbf{R}, B| - |\mathbf{R} + \mathbf{r}_x - \mathbf{e}_y, B\rangle \langle \mathbf{R}, A| \\
& \left. - |\mathbf{R} + \mathbf{r}_x + \mathbf{e}_y, A\rangle \langle \mathbf{R}, B| + |\mathbf{R} + \mathbf{r}_x + \mathbf{e}_y, B\rangle \langle \mathbf{R}, A| \right), \quad (\text{S44})
\end{aligned}$$

$$\begin{aligned}
H_{2D}^{\text{AII}(3)} = & -ic \sum_{\mathbf{R}} \sum_{\mathbf{r}_y=-\mathbf{e}_y, \mathbf{e}_y} \left( |\mathbf{R} - \mathbf{e}_x + \mathbf{r}_y, A\rangle \langle \mathbf{R}, A| - |\mathbf{R} - \mathbf{e}_x + \mathbf{r}_y, B\rangle \langle \mathbf{R}, B| \right) \\
& - |\mathbf{R} + \mathbf{e}_x + \mathbf{r}_y, A\rangle \langle \mathbf{R}, A| + |\mathbf{R} + \mathbf{e}_x + \mathbf{r}_y, B\rangle \langle \mathbf{R}, A| \\
& - |\mathbf{R} + \mathbf{r}_y, A\rangle \langle \mathbf{R}, A| + |\mathbf{R} + \mathbf{r}_y, B\rangle \langle \mathbf{R}, B| \\
& + |\mathbf{R} + 2\mathbf{e}_x + \mathbf{r}_y, A\rangle \langle \mathbf{R}, A| - |\mathbf{R} + 2\mathbf{e}_x + \mathbf{r}_y, B\rangle \langle \mathbf{R}, B| \Big), \quad (\text{S45})
\end{aligned}$$

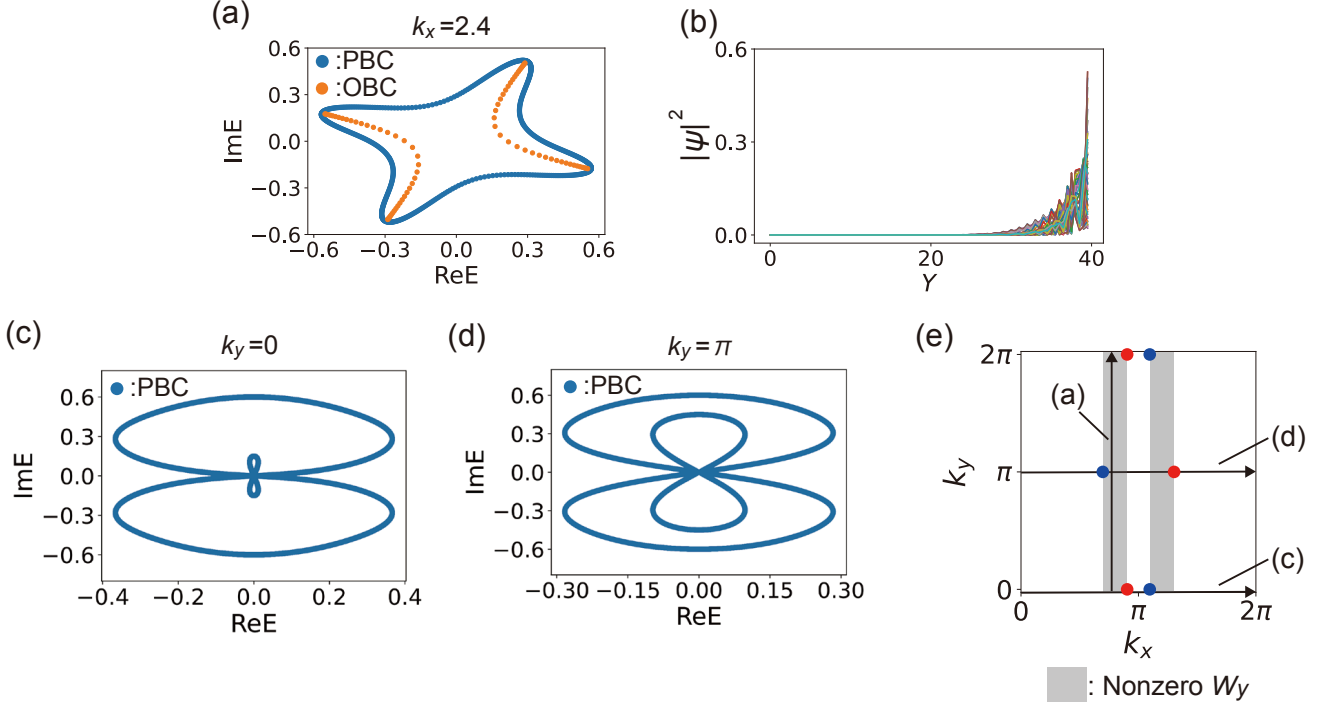


FIG. S8. Energy spectra of  $H_{2D}^{AII}(\mathbf{k})$  with the parameters  $t = v = 0.15$  and  $c = 0.05$ . (a) The energy spectra under the PBC in the  $x$  direction. We apply the PBC in the  $y$  direction and the OBC in the  $y$  direction. (b) The spatial distributions of  $|\psi_n|^2$  for all the right eigenstates  $\psi_n$  under the OBC in (a). The system size in the  $y$  direction is 40. (c), (d) The energy spectra under the full PBC. The wave vector is fixed to (c)  $k_y = 0$  and (d)  $k_y = \pi$ . (e) The positions of the 2D Weyl point of  $H_{2D}^{AII}(\mathbf{k})$  and the regions with the nonzero winding number  $W_y(k_x)$  in the Brillouin zone. The arrows indicate the direction of integration of the winding number. The colors of the points represent the opposite chirality of the Weyl points.

where  $\mathbf{e}_x$  and  $\mathbf{e}_y$  are the unit vectors in the  $x$  and  $y$  directions, respectively, and  $\mathbf{R}$  is the position of the unit cell. We obtain the  $2 \times 2$  Bloch Hamiltonian

$$H_{2D}^{AII}(\mathbf{k}) = -it(1 - e^{-ik_x})(1 - e^{-ik_y} + 0.5e^{ik_y})\sigma_x - 2iv(1 + e^{-ik_x})(1 - i \sin k_y)\sigma_y + 4c(1 - e^{-ik_x}) \sin k_x \cos k_y \sigma_z, \quad (S46)$$

where  $\sigma_i$  ( $i = x, y, z$ ) are Pauli matrices representing the two degree of freedom  $A$  and  $B$ . The model satisfies the condition for the screw symmetry  $g = \{C_{2x}|\hat{\mathbf{x}}/2\}$  with  $c_g = -1$ , which is described as

$$iA_g^{\mathbf{k}} H_{2D}^{AII}(\mathbf{k}) = \left( i e^{ik_x} A_g^{C_{2x}\mathbf{k}} H_{2D}^{AII}(C_{2x}\mathbf{k}) \right)^\dagger, A_g^{\mathbf{k}} = -i e^{-ik_y} \sigma_x. \quad (S47)$$

Correspondingly, we have

$$B_g^{\mathbf{k}} = -(e^{ik_x} A_g^{C_{2x}\mathbf{k}})^\dagger = -i e^{-i(k_x + k_y)} \sigma_x. \quad (S48)$$

Our model also has time-reversal symmetry given by

$$\mathcal{T} H_{2D}^{AII*}(\mathbf{k}) \mathcal{T}^{-1} = H_{2D}^{AII}(-\mathbf{k}), \quad \mathcal{T} = i\sigma_y, \quad (S49)$$

which corresponds to class AII. Therefore, the symmetry-enforced NHSE occurs in this model.

To confirm the symmetry-enforced NHSE, we calculate energy spectra of  $H_{2D}^{AII}(\mathbf{k})$  under the PBC in the  $x$  direction. Figure S8(a) shows the energy spectra under the PBC and under the OBC in the  $y$  direction. Indeed, we can find that the spectrum under the full PBC gives the nonzero  $W_y(k_x)$  in the Brillouin zone because  $H_{2D}^{AII}(\mathbf{k})$  satisfies the conditions of the symmetry and the matrix size. As a result, we can also find eigenstates localized at the edge under the OBC in the  $y$  direction [Fig. S8(b)]. Moreover, we can also see symmetry-enforced gaplessness on the lines  $k_y = 0$  and  $k_y = \pi$ , as shown in Figs S8(c) and S8(d).

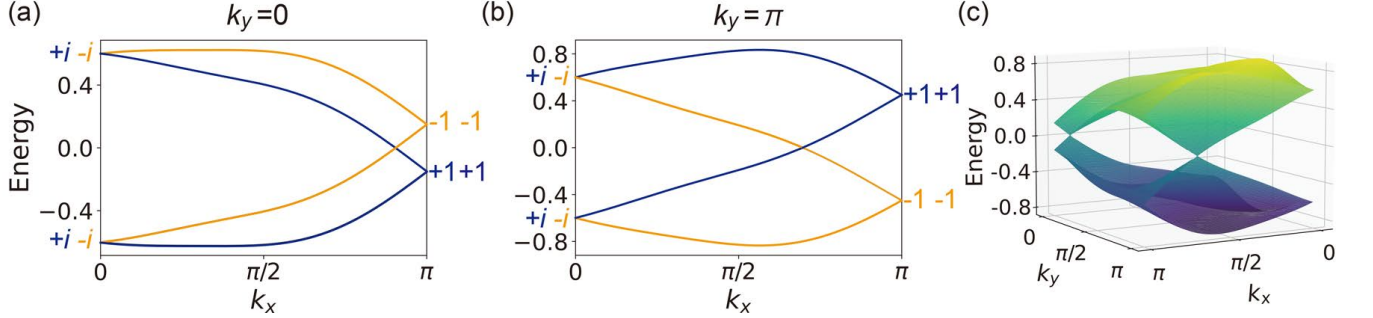


FIG. S9. Band structures of  $\tilde{H}_{2D}^{CH}(\mathbf{k})$  with the parameters  $t = v = 0.15$  and  $c = 0.05$ . (a), (b) The energy spectra with the screw  $\{C_{2x}|\hat{\mathbf{x}}/2\}$  symmetry eigenvalues,  $\pm i \exp(-i(k_y + \frac{k_x}{2}))$  along the screw invariant lines with (a)  $k_y = 0$  and (b)  $k_y = \pi$ . (c) The band structures in a quarter of the Brillouin zone.

To see the origin clearly, we find Weyl points of the doubled Hermitian Hamiltonian

$$\begin{aligned} \tilde{H}_{2D}^{CH}(\mathbf{k}) &= \begin{pmatrix} H_{2D}^{AII}(\mathbf{k}) & H_{2D}^{AII}(\mathbf{k}) \\ H_{2D}^{AII}(\mathbf{k})^\dagger & H_{2D}^{AII}(\mathbf{k}) \end{pmatrix} \\ &= t(1.5(1 - \cos k_x) \sin k_y + \sin k_x(1 - 0.5 \cos k_y))\tau_x \otimes \sigma_x \\ &\quad + t((1 - \cos k_x)(1 - 0.5 \cos k_y) - 1.5 \sin k_x \sin k_y)\tau_y \otimes \sigma_x \\ &\quad - 2v((1 + \cos k_x) \sin k_y + \sin k_x) \tau_x \otimes \sigma_y + 2v((1 + \cos k_x) - \sin k_x \sin k_y)\tau_y \otimes \sigma_y \\ &\quad + 4c(1 - \cos k_x) \sin k_x \cos k_y \tau_x \otimes \sigma_z - 4c \sin^2 k_x \cos k_y \tau_y \otimes \sigma_z, \end{aligned} \quad (\text{S50}) \quad (\text{S51})$$

where  $\tau_i$  ( $i = x, y, z$ ) are Pauli matrices. The doubled Hermitian Hamiltonian has the screw rotation symmetry  $\tilde{U}_g^{\mathbf{k}} \tilde{H}_{2D}^{CH}(\mathbf{k}) \tilde{U}_g^{\mathbf{k}\dagger} = \tilde{H}_{2D}^{CH}(C_{2x}\mathbf{k})$ , where  $\tilde{U}_g^{\mathbf{k}}$  is represented by

$$\tilde{U}_g^{\mathbf{k}} = -ie^{-ik_y} \begin{pmatrix} e^{-ik_x} & \\ & 1 \end{pmatrix} \otimes \sigma_x. \quad (\text{S52})$$

Indeed, 2D Weyl points can be found on the screw-invariant lines [Fig. S8(e)]. Thus, the winding number can be nonzero between the Weyl points, as shown in Fig. S8(e). Figures S9(a) and S9(b) show the energy spectra and the screw-symmetry eigenvalues along the screw invariant lines ( $k_y = 0, \pi$ ). In addition, Fig. S9(c) shows the band structure in a quarter of the Brillouin zone. The occupied states with the screw-symmetry eigenvalues require the Weyl point on the screw invariant lines with  $k_y = 0$  and  $k_y = \pi$ . Because these Weyl points are enforced by the screw symmetry and time-reversal symmetry, the NHSE in Fig. S8(a) cannot disappear when  $H_{2D}(\mathbf{k})$  has the symmetry condition [Eq. (S47)] and time-reversal symmetry [Eq. (S49)].

#### D. class AI and class AI<sup>†</sup>

Lastly, we comment on class AI and class AI<sup>†</sup> [10]. Similarly to class A, we consider non-Hermitian Hamiltonians satisfying the conditions in (S25) in class AI and class AI<sup>†</sup>. When a non-Hermitian Hamiltonian belongs to class AI (AI<sup>†</sup>), the doubled Hermitian Hamiltonian belongs to class BDI (CI). In both classes, the doubled Hermitian Hamiltonian has time-reversal ( $\tilde{T}$ ) symmetry. In a similar way to class A, the screw symmetry of the doubled Hermitian Hamiltonian enforces double degeneracy on the screw-invariant lines ( $k_y = 0, \pi$ ) when the matrix size is  $4M + 2$  [9]. However, because of time-reversal symmetry, the two states form the double degeneracy along the  $k_x = \pi$  line because  $(\tilde{T}\{C_{2x}|\hat{\mathbf{x}}/2\})^2 = e^{-ik_x}$ . Thus, the gap-closing line appears at zero energy instead of 2D Weyl points in both class BDI and class CI, and therefore nonzero winding numbers are not enforced in these cases.

**Supplemental Material V. DETAILS OF CALCULATIONS OF THE 3D SYMMETRY-ENFORCED NHSE**

In this section, we describe details of band topology for the 3D NHSE in the main text. To do so, we first see a 3D doubled Hermitian Hamiltonian obtained from  $H_{3D}(\mathbf{k})$  in Eq. (7) in the main text, which is given by

$$\tilde{H}_{3D}(\mathbf{k}) = \begin{pmatrix} & H_{3D}(\mathbf{k}) \\ H_{3D}^\dagger(\mathbf{k}) & \end{pmatrix}. \quad (\text{S53})$$

The doubled Hermitian Hamiltonian  $\tilde{H}_{3D}(\mathbf{k})$  is given by

$$\begin{aligned} \tilde{H}_{3D}(\mathbf{k}) = & V_1(\mathbf{k}_{\parallel}) \left( \frac{t_0}{4} \sin k_z \tau_y \otimes \sigma_0 + \frac{t_a}{4} \tau_x \otimes \sigma_0 + \frac{t_b}{8} \sin k_z \tau_y \otimes \sigma_x + \frac{t_b}{8} (1 - \cos k_x) \tau_y \otimes \sigma_y \right) \\ & + V_2(\mathbf{k}_{\parallel}) \left( -\frac{t_0}{4} \sin k_z \tau_x \otimes \sigma_0 + \frac{t_a}{4} \tau_y \otimes \sigma_0 - \frac{t_b}{8} \sin k_z \tau_x \otimes \sigma_x - \frac{t_b}{8} (1 - \cos k_z) \tau_x \otimes \sigma_y \right) \\ & + V_3(\mathbf{k}_{\parallel}) \left( -\frac{t_c}{8} (1 + \cos k_z) \tau_y \otimes \sigma_y + \frac{t_c}{8} \sin k_z \tau_y \otimes \sigma_x - \frac{t_d}{8} \sin k_z \tau_x \otimes \sigma_y + \frac{t_d}{8} (1 - \cos k_z) \tau_x \otimes \sigma_x \right) \\ & + V_4(\mathbf{k}_{\parallel}) \left( -\frac{t_c}{8} (1 + \cos k_z) \tau_x \otimes \sigma_y + \frac{t_c}{8} \sin k_z \tau_x \otimes \sigma_x + \frac{t_d}{8} \sin k_z \tau_y \otimes \sigma_y - \frac{t_d}{8} (1 - \cos k_z) \tau_y \otimes \sigma_x \right), \end{aligned} \quad (\text{S54})$$

with

$$\begin{aligned} V_1(\mathbf{k}_{\parallel}) &= 1 + \cos k_x + \cos k_y + \cos(k_x + k_y), \\ V_2(\mathbf{k}_{\parallel}) &= \sin k_x + \sin k_y + \sin(k_x + k_y), \\ V_3(\mathbf{k}_{\parallel}) &= (\cos k_x - \cos 2k_x)(1 - \cos k_y) - (\sin k_x + \sin 2k_x) \sin k_y \\ &\quad - (\cos k_y - \cos 2k_y)(1 - \cos k_x) + (\sin k_y + \sin 2k_y) \sin k_x, \\ V_4(\mathbf{k}_{\parallel}) &= (\cos k_x - \cos 2k_x) \sin k_y + (\sin k_x + \sin 2k_x)(1 - \cos k_y) \\ &\quad - (\cos k_y - \cos 2k_y) \sin k_x - (\sin k_y + \sin 2k_y)(1 - \cos k_x), \end{aligned} \quad (\text{S55})$$

where  $\tau_i$  and  $\sigma_i$  ( $i = x, y, z$ ) are Pauli matrices and  $\tau_0$  and  $\sigma_0$  are the identity matrices. The doubled Hermitian Hamiltonian corresponds to a 3D tight-binding model on a primitive orthorhombic lattice with the four sublattices at  $\mathbf{r}_\alpha = (1/4, 1/4, 0)$ ,  $(1/4, 1/4, 1/2)$ ,  $(3/4, 3/4, 0)$ , and  $(3/4, 3/4, 1/2)$  in each unit cell [12]. In the model, the Pauli matrices  $\sigma_i$  represent  $z = 0$  and  $z = 1/2$  sublattices, and  $\tau_i$  represents the  $(x, y) = (1/4, 1/4)$  and  $(x, y) = (3/4, 3/4)$  sublattices.

To see the band topology, we discuss symmetries of the doubled Hermitian Hamiltonian  $\tilde{H}_{3D}(\mathbf{k})$  by using the Seitz notation. Let  $\mathbf{x}$ ,  $\mathbf{y}$ , and  $\mathbf{z}$  denote the lattice vectors in the  $x$ ,  $y$ , and  $z$  directions, respectively. The doubled Hermitian Hamiltonian belongs to space group  $P4/ncc$  (No. 130) generated by  $\{I|\mathbf{0}\}$ ,  $\{C_{4z}|\frac{1}{2}\hat{\mathbf{x}}\}$ ,  $\{C_{2y}|\frac{1}{2}\hat{\mathbf{y}} + \frac{1}{2}\hat{\mathbf{z}}\}$ , and  $\{C_{2z}|\frac{1}{2}\hat{\mathbf{x}} + \frac{1}{2}\hat{\mathbf{y}}\}$ , where  $I$  represents the inversion, and  $C_{4z}$  represents the fourfold rotation around the  $z$  axis, and  $C_{2y}$  and  $C_{2z}$  represents the twofold rotation around the  $y$  and the  $z$  axes, respectively. The symmetry representations  $\tilde{U}_g^{\mathbf{k}}$

Symmetry operation	$c_g$	$A_g^{\mathbf{k}}$	$B_g^{\mathbf{k}}$	Symmetry relation
$\{I \mathbf{0}\}$	-1	$e^{-i(k_x+k_y+k_z)}\sigma_x$	$e^{-i(k_x+k_y+k_z)}\sigma_x$	$A_g^{\mathbf{k}}H_{3D}(k_x, k_y, k_z) = H_{3D}^\dagger(-k_x, -k_y, -k_z)B_g^{\mathbf{k}}$
$\{C_{4z} \frac{1}{2}\hat{\mathbf{x}}\}$	1	$\sigma_0$	$e^{-ik_y}\sigma_0$	$A_g^{\mathbf{k}}H_{3D}(k_x, k_y, k_z) = H_{3D}(-k_y, k_x, k_z)B_g^{\mathbf{k}}$
$\{C_{2y} \frac{1}{2}\hat{\mathbf{y}} + \frac{1}{2}\hat{\mathbf{z}}\}$	-1	$\begin{pmatrix} e^{-ik_x} & \\ & e^{-i(k_x+k_z)} \end{pmatrix}$	$\begin{pmatrix} e^{-i(k_x+k_y)} & \\ & e^{-i(k_x+k_y+k_z)} \end{pmatrix}$	$A_g^{\mathbf{k}}H_{3D}(k_x, k_y, k_z) = H_{3D}^\dagger(-k_x, k_y, -k_z)B_g^{\mathbf{k}}$
$\{C_{2z} \frac{1}{2}\hat{\mathbf{x}} + \frac{1}{2}\hat{\mathbf{y}}\}$	1	$\sigma_0$	$e^{-i(k_x+k_y)}\sigma_0$	$A_g^{\mathbf{k}}H_{3D}(k_x, k_y, k_z) = H_{3D}(-k_x, -k_y, k_z)B_g^{\mathbf{k}}$
$\tilde{T}$	-	-	-	$H_{3D}^*(k_x, k_y, k_z) = H_{3D}(-k_x, -k_y, -k_z)$

Table S I. The symmetry relations of the 3D non-Hermitian Hamiltonian  $H_{3D}(\mathbf{k})$ .

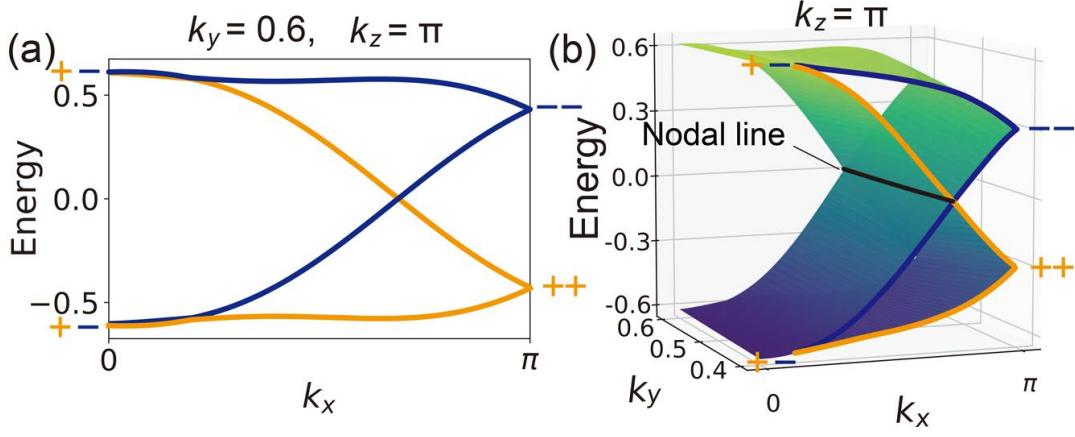


FIG. S10. Nodal lines in the doubled Hermitian Hamiltonian  $\tilde{H}_{3D}(\mathbf{k})$ . We choose the parameters  $t_0 = 0.125$ ,  $t_a = 0.1$ ,  $t_b = t_d = 0.05$ , and  $t_c = 0.025$ . (a) The energy spectra on the  $(k_x, k_z) = (0.6, \pi)$  line. In the figure,  $\pm$  denotes the sign of the glide symmetry eigenvalues  $\pm e^{-\frac{i}{2}(k_x+k_y)}$ . (b) The band structures on the  $k_z = \pi$  plane.

are

$$\begin{aligned}
 \tilde{U}_{\{I|\mathbf{0}\}}^{\mathbf{k}} &= e^{-i(k_x+k_y+k_z)}\tau_x \otimes \sigma_x, \\
 \tilde{U}_{\{C_{4z}|\frac{1}{2}\hat{x}\}}^{\mathbf{k}} &= \begin{pmatrix} 1 & \\ & e^{-ik_y} \end{pmatrix} \otimes \sigma_0, \\
 \tilde{U}_{\{C_{2y}|\frac{1}{2}\hat{y}+\frac{1}{2}\hat{z}\}}^{\mathbf{k}} &= \begin{pmatrix} & e^{-i(k_x+k_y)} \\ e^{-ik_x} & \end{pmatrix} \otimes \begin{pmatrix} 1 & \\ & e^{-ik_z} \end{pmatrix}, \\
 \tilde{U}_{\{C_{2z}|\frac{1}{2}\hat{x}+\frac{1}{2}\hat{y}\}}^{\mathbf{k}} &= \begin{pmatrix} 1 & \\ & e^{-i(k_x+k_y)} \end{pmatrix} \otimes \sigma_0.
 \end{aligned} \tag{S56}$$

We can understand that the crystal symmetries stem from symmetry relations in Eq. (S19). Their projective factors can be calculated from the symmetry representations. The relations are summarized in Table S I. Furthermore, the model  $H_{3D}(\mathbf{k})$  has time-reversal symmetry  $H_{3D}^*(\mathbf{k}) = H_{3D}(-\mathbf{k})$ , which means that it belongs to class AI. Thus,  $\tilde{H}_{3D}(\mathbf{k})$  has time-reversal symmetry  $\tilde{T}\tilde{H}_{3D}(\mathbf{k})\tilde{T}^{-1} = \tilde{H}_{3D}(-\mathbf{k})$  with  $\tilde{T} = K$ , which satisfies  $\tilde{T}^2 = 1$ .

Importantly, when time-reversal symmetry with  $\tilde{T}^2 = 1$  is present, the space group  $P4/ncc$  realizes nodal lines enforced by glide reflection symmetry [12]. The glide symmetry is given by  $G = \{M_z|\frac{1}{2}\hat{x}+\frac{1}{2}\hat{y}\} = \{C_{2z}|\frac{1}{2}\hat{x}+\frac{1}{2}\hat{y}\}\{I|\mathbf{0}\}$ , where  $M_z$  is mirror reflection with the  $x$ - $y$  mirror plane. The projective factor of the glide symmetry is  $c_G = -1$ . We show that  $\tilde{H}_{3D}(\mathbf{k})$  can also host a symmetry-enforced nodal line on the glide-invariant plane  $k_z = \pi$  due to  $c_G = -1$  even when chiral symmetry exists. The eigenstates are labeled by the glide reflection eigenvalues  $\pm e^{-\frac{i}{2}(k_x+k_y)}$  on the glide-invariant plane  $k_z = \pi$ . Figure S10(a) shows that the eigenstates with the glide eigenvalues need to exchange between  $k_x = 0$  and  $k_x = \pi$  on the glide-invariant  $k_x$ - $k_y$  plane, resulting in the gapless point. Furthermore, since  $c_G = -1$ , the two doubly-degenerate states and the chiral partner have glide eigenvalues of the opposite sign [Fig. S10]. The eigenvalue exchange enforces band degeneracy at zero energy due to chiral symmetry because the matrix size of  $\tilde{H}_{3D}(\mathbf{k})$  is 4. In general, the symmetry-enforced nodal line can appear at zero energy if the matrix size is  $8M + 4$ . The mechanism is similar to symmetry-enforced 2D Weyl point in time-reversal-invariant classes with  $\mathcal{T}^2 = -1$  in Fig. S9. The degeneracy forms the nodal line on the glide-invariant plane  $k_z = \pi$  [Fig. S10(b)].

From the above discussion, we can understand why  $H_{3D}(\mathbf{k})$  shows the symmetry-enforced NHSE. Because the doubled Hermitian Hamiltonian has the symmetry-enforced nodal line, it results in a nonzero winding number. Then, we can always find a path for the nonzero winding number along the  $k_z$  direction. As a result, the symmetry-enforced NHSE happens under the OBC in the  $z$  direction and under the PBC in the other directions.

[1] K. Zhang, Z. Yang, and C. Fang, Universal non-Hermitian skin effect in two and higher dimensions, Nat. Commun. **13**, 2496 (2022).

- [2] N. Okuma, K. Kawabata, K. Shiozaki, and M. Sato, Topological origin of non-hermitian skin effects, *Phys. Rev. Lett.* **124**, 086801 (2020).
- [3] C.-K. Chiu, J. C. Y. Teo, A. P. Schnyder, and S. Ryu, Classification of topological quantum matter with symmetries, *Rev. Mod. Phys.* **88**, 035005 (2016).
- [4] A. Altland and M. R. Zirnbauer, Nonstandard symmetry classes in mesoscopic normal-superconducting hybrid structures, *Phys. Rev. B* **55**, 1142 (1997).
- [5] C. Le, Z. Yang, F. Cui, A. P. Schnyder, and C.-K. Chiu, Generalized fermion doubling theorems: Classification of two-dimensional nodal systems in terms of wallpaper groups, *Phys. Rev. B* **106**, 045126 (2022).
- [6] S. Matsuura, P.-Y. Chang, A. P. Schnyder, and S. Ryu, Protected boundary states in gapless topological phases, *New J. of Phys.* **15**, 065001 (2013).
- [7] K. Shiozaki and S. Ono, Symmetry indicator in non-Hermitian systems, *Phys. Rev. B* **104**, 035424 (2021).
- [8] L. Michel and J. Zak, Connectivity of energy bands in crystals, *Phys. Rev. B* **59**, 5998 (1999).
- [9] S. M. Young and C. L. Kane, Dirac Semimetals in Two Dimensions, *Phys. Rev. Lett.* **115**, 126803 (2015).
- [10] K. Kawabata, K. Shiozaki, M. Ueda, and M. Sato, Symmetry and Topology in Non-Hermitian Physics, *Phys. Rev. X* **9**, 041015 (2019).
- [11] B. J. Wieder and C. L. Kane, Spin-orbit semimetals in the layer groups, *Phys. Rev. B* **94**, 155108 (2016).
- [12] R. Takahashi, M. Hirayama, and S. Murakami, Spinless hourglass nodal-line semimetals, *Phys. Rev. B* **96**, 155206 (2017).